Monthly Notices of the ROYAL ASTRONOMICAL SOCIETY
MNRAS **547,** 1–23 (2026) https://doi.org/10.1093/mnras/staf2239
Advance Access publication 2025 December 19

The Nearby Evolved Stars Survey – IV. Mapping cold gas in the circumstellar envelopes of evolved stars with ^{12}CO and ^{13}CO ($J = 1 \rightarrow 0$) emission

K. Amada [1★] S. Fukaya,[2] H. Imai,[2,3] P. Scicluna,[4,5] N. Hirano,[6] A. Trejo-Cruz,[6,7] S. Zeegers,[8,9] F. Kemper [10,11,12] Jinhua He,[13,14,15] S. Srinivasan,[7] I. McDonald [16,17] J. P. Marshall [6] J. A. Toalá [7] S. H. J. Wallström,[6,18] O. C. Jones [19] A. A. Zijlstra,[16] J. Cami [20,21,22] Hyosun Kim [23] R. Wesson [24] C. J. R. Clark [25] T. Dharmawardena,[6,26] G. Rau [27,28] and H. Shinnaga [2] NESS collaboration

Affiliations are listed at the end of the paper

Accepted 2025 November 25. Received 2025 October 31; in original form 2024 November 29

ABSTRACT

We have performed mapping observations of 42 AGB stars, of which 23 and 14 stars were detected in ^{12}CO and ^{13}CO ($J = 1 \rightarrow 0$) emission, respectively, using 45 m telescope of Nobeyama Radio Observatory. Our aim is to reveal distributions of extended cold gas in circumstellar envelopes and test a possibility of detecting shell structures with high ^{12}CO/^{13}CO ratios caused by thermal pulses and third dredge-ups. By comparing our maps with those of ^{12}CO ($J = 3 \rightarrow 2$) emission obtained with James Clerk Maxwell Telescope at the same angular resolution, we found that envelopes of ^{12}CO ($J = 1 \rightarrow 0$) emission has at least twice the sizes of ^{12}CO ($J = 3 \rightarrow 2$) emission. Among 14 stars detected in both ^{12}CO and ^{13}CO emission, nine stars show radial variations of ^{12}CO/^{13}CO ratio along radial direction in their envelopes, which is likely caused by selective photodissociation by interstellar ultraviolet radiation, not thermal pulses or third dredge ups. Based on radiative transfer simulations, we conclude that optical depths are small (typically $\tau \lesssim 0.5$), ruling out the possibility that the absence of detected shells in our data is due to optical depth. This implies no signatures of thermal pulses or third dredge ups in the last ∼1500–13 000 yr. We further confirmed aspherical envelope morphologies of *o* Cet, WX Psc, and RAFGL 618, which were likely formed by bipolar outflows and photodissociation. The elongated morphology of SV Peg that we newly found is subject to study.

Key words: stars: AGB and post-AGB – stars: mass-loss – stars: winds, outflows.

1 INTRODUCTION

The asymptotic giant branch (AGB) represents one of the most advanced evolutionary phases of low- to intermediate-mass stars ($M_{\rm i} \sim 1$–8 M$_\odot$; e.g. F. Herwig 2005). AGB stars release material from their surfaces at a rate of $\sim 10^{-8}$ M$_\odot$ yr^{-1} to 10^{-4} M$_\odot$ yr^{-1} (e.g. H. J. Habing & H. Olofsson 2004). This mass loss forms a circumstellar envelope (CSE) of gas and dust, which is often assumed to be spherically symmetric as a result of isotropic outflows (e.g. A. Castro-Carrizo et al. 2010). However, time variation in mass-loss rate associated with physical phenomena in an AGB star can significantly affect CSE morphologies (e.g. H. Olofsson et al. 1990; K. P. Schröder, J. M. Winters & E. Sedlmayr 1999). External effects, such as those due to the presence of a binary companion, can also play an important role in shaping the CSE, producing spiral patterns, disks, or bipolar outflows (e.g. L. Decin et al. 2020).

In the interior of an AGB star, increase in helium causes thermal pulses as a result of a helium flash triggered by geometrical and thermal instabilities. These thermal pulses induce convection that dredges up carbon-rich material from the vicinity of the central core to the stellar surface (third dredge up), and eventually a star evolves into a carbon-rich star with an abundance ratio C/O > 1. In contrast, more massive AGB star ($M_{\rm i} \sim 5$–8 M$_\odot$) remains an oxygen-rich star with C/O < 1 due to hot-bottom-burning (A. I. Karakas & J. C. Lattanzio 2014). Therefore, thermal pulses and third dredge up affect essentially the chemical evolution of AGB stars.

Thermal pulses also change stellar luminosity, radius, and surface effective temperature (O. R. Pols et al. 2001). During a pulse, the luminosity decreases rapidly, followed by a brief luminosity peak, and then gradually returns to pre-thermal pulse value (J. Wagenhuber & M. A. T. Groenewegen 1998). This increase in luminosity enhances both wind velocity and mass-loss rate, resulting that faster wind sweeps up the previously ejected slower wind. This interaction produces a geometrically thin and dense detached shell-like structure of gas (and dust) with a high ^{12}C/^{13}C ratio ($\gtrsim 20$) (e.g. H. Olofsson et al. 1990, 1993; M. Steffen, R. Szczerba & D. Schoenberner 1998; K. P. Schröder et al. 1999; M. Steffen & D. Schönberner 2000; F. L. Schöier, M. Lindqvist & H. Olofsson 2005; L. Mattsson, S. Höfner & F. Herwig 2007; W. H. T. Vlemmings et al. 2013). However, this scenario is not quantitatively consistent with observed CSEs and detached-shell properties. In the detached shell of R Scl, the mass-loss rate during the thermal pulse was more than 30 times higher than that before the thermal pulse, which is

★ E-mail: keiamada.0304@gmail.com

significantly larger than a enhancement predicted by models (M. Maercker et al. 2012).

Currently, the number of AGB stars with confirmed detached shells is limited to ∼ 10 stars, all of which are C-rich stars (J. H. Kastner & E. Wilson 2021). Therefore, it is important to discover new detached shells and investigate their properties. In this context, observations in ground-state CO emission line using single-dish telescopes are expected to identify previously undetected detached shells with a high ^{12}CO/^{13}CO ratio because such observations are sensitive to spatially extended and cold CSEs rather than those in excited CO lines.

However, note that CO isotopologues in CSEs undergo selective photodissociation by ultraviolet (UV) radiation, in which ^{13}CO molecules are more easily destroyed than ^{12}CO, leading to elevated ^{12}CO/^{13}CO ratios. In fact, in the case of R Scl, HCN emission line observations and their excitation analysis suggested that HCN molecule is more resistant to photodissociation than CO molecule, and that the CO isotope ratio is affected by photodissociation. Furthermore, M. Saberi et al. (2020) performed simulations taking into account UV radiation from the interstellar medium and demonstrated that the ^{12}CO/^{13}CO ratio increases toward outer CSE due to selective photodissociation. Therefore, a high ^{12}CO/^{13}CO ratio in CSE can be caused by not only thermal pulses and third dredge-up but also selective photodissociation. However, in the former case, an enhancement in gas density is expected at the detached shell radius. Accordingly, if a observed high ^{12}CO/^{13}CO ratio originates from a thermal pulse and third dredge-up, a corresponding increase in CO line intensity should be detectable, allowing us to distinguish between the two scenarios.

The Nearby Evolved Stars Survey (NESS)[1] project aims to observe a volume-complete sample of ∼850 evolved stars within 3 kpc in CO ($J = 2 \rightarrow 1$) and CO ($J = 3 \rightarrow 2$) emission lines and 870 and 450 μm continuum mainly using SCUBA2 (W. S. Holland et al. 2013) and heterodyne receivers on the James Clerk Maxwell Telescope (JCMT) (P. Scicluna et al. 2022). Scientific goals of NESS are (i) to measure the total rate at which circumstellar material is released from evolved stars to interstellar medium, (ii) to study the physical and chemical properties of enriched materials in CSEs, and (iii) to explore the physics of onset and time evolution of dusty stellar winds. For more details and a review of this project, see P. Scicluna et al. (2022).

This paper presents, as a part of the NESS project, single-point and mapping observations in CO ($J = 1 \rightarrow 0$) emission using the 45 m telescope of Nobeyama Radio Observatory (NRO), so-called NESS–NRO, at the same angular resolution as the NESS–JCMT observations in CO ($J = 3 \rightarrow 2$) emission and 870 μm continuum. Previous mapping observations of AGB stars in CO ($J = 1 \rightarrow 0$) emission have been conducted with the IRAM Plateau de Bure interferometer (PdBI) or a combination of the IRAM PdBI with IRAM 30 m radio telescope, but ^{13}CO emission was not observed (H. Olofsson et al. 2000; A. Castro-Carrizo et al. 2010). Other mapping observations, except for the NESS project in CO emission, have been conducted using radio interferometers, but extended components of envelopes were filtered out (e.g. S. Ramstedt et al. 2020; C. A. Gottlieb et al. 2022). For example, in DEATHSTAR observations, maximum recoverable scale using the Atacama Compact Array was, on average, 25″ ± 4″ in Band 6 and 18 arcsec ± 2 arcsec in Band 7 (S. Ramstedt et al. 2020). By contrast, our NESS–NRO observations use On-The-Fly mapping mode with a single-dish telescope and are sensitive to more extended components (map size: 170″ × 170″). Furthermore, CO ($J = 3 \rightarrow 2$ and $J = 2 \rightarrow 1$) emission trace warmer gas in inner regions of CSEs, whereas CO ($J = 1 \rightarrow 0$) emission is more sensitive to colder and more extended gas. Therefore, our ^{12}CO and ^{13}CO ($J = 1 \rightarrow 0$) simultaneous observations with a single-dish telescope are expected to probe older mass-loss history and search for signatures of detached shell with a ^{12}C/^{13}C ratio derived from a ^{12}CO/^{13}CO line ratio.

This paper presents mainly CSEs mapped using the 45 m telescope of NRO and discusses their cold gas distribution and radial changes of ^{12}CO/^{13}CO intensity ratios as a possible signature of thermal pulse. In addition, some aspherical morphologies of CSEs mapped in ^{12}CO and ^{13}CO ($J = 1 \rightarrow 0$) lines are highlighted.

2 OBSERVATIONS

2.1 NESS-NRO samples

NESS has investigated mass-loss rates and CSE morphologies for a large number of nearby evolved stars (T. E. Dharmawardena et al. 2018; P. Scicluna et al. 2022). Regarding distances, sample selection was originally based on the analyses by I. McDonald, A. A. Zijlstra & M. L. Boyer (2012) and I. McDonald, A. A. Zijlstra & R. A. Watson (2017), which employed parallaxes from *Hipparcos* (F. Leeuwen 2007) and the *Tycho–Gaia* Astrometric Solution (D. Michalik, L. Lindegren & D. Hobbs 2015), respectively. In addition, bolometric luminosities were also used (P. Scicluna et al. 2022). A threshold on parallax uncertainty ($\sigma_{\varpi}/\varpi < 0.25$) was applied to ensure reliable distances, and ∼850 sources that satisfied this criterion were selected. Details of this sample selection and the luminosity-based analysis can be found in Section 2.2 of P. Scicluna et al. (2022).

More recently, improved distances based on Gaia DR3 dataset and maser parallax measurements have become available. We mainly adopt the catalogue by M. Andriantsaralaza et al. (2022), which provides the most reliable distances to AGB stars based on maser and Gaia DR3 parallaxes. When a distance to the targets was not found in this catalogue, we used Gaia EDR3-based distances provided by C. A. L. Bailer-Jones et al. (2021). For targets not included in either catalogue, we adopted distances based on *Hipparcos* parallaxes (F. Leeuwen 2007) or those derived using the luminosity distribution of evolved stars in the Large Magellanic Cloud as described in P. Scicluna et al. (2022).

We have carried out single-point observations towards 208 of the ∼850 NESS sources in early semesters of the NESS-NRO project in order to detect CO ($J = 1 \rightarrow 0$) emission lines towards as many stars as possible. From these stars, we then selected a statistically sufficient number (>20) of stars with bright ^{12}CO emission ($T_{\rm A} \geq 0.5$ K in main-beam temperature) for mapping observations.

2.2 Single-point observations

We have conducted single-point observations in ^{12}CO, ^{13}CO, and C^{18}O ($J = 1 \rightarrow 0$) emission lines over four semesters (March–April 2018, March–April 2019, December 2019–January 2020, and December 2021–February 2022) using the NRO 45 m telescope. Because no C^{18}O emission was detected in any of targets, this paper will only focus on the ^{12}CO and ^{13}CO lines at the rest frequencies of 115.271204 and 110.201354 GHz, respectively. The angular resolution is ∼ 15 ″, which is equal to that of the NESS-JCMT observations in CO ($J = 3 \rightarrow 2$) emission and 870 μm continuum.

We used FOur-beam REceiver System on the 45 m Telescope (FOREST; T. Minamidani et al. 2016), in which two of four beams were used in position switch (on–on) mode. The beam separation of FOREST is 50 arcsec on the sky plane. The ^{12}CO and ^{13}CO lines were

[1] https://evolvedstars.space/

observed simultaneously in upper- and lower-sidebands, respectively. The main-beam efficiencies were 35 per cent in 115 GHz and 39 per cent in 110 GHz in the second semester and 39 per cent in both frequencies in the third and fourth semesters. For the first semester, main beam efficiency was not measured by the observatory, therefore we adopted the values provided in 2017 (45 per cent and 43 per cent, respectively).

For spectroscopy, Spectral Analysis Machine for the 45 m telescope (SAM45; T. Kamazaki et al. 2012) was used, yielding data with a bandwidth of 1000 MHz and a frequency resolution of 244 kHz. These values correspond to velocity coverages of 2600 and 2720 km s^{-1} and resolutions of 0.63 and 0.66 km s^{-1} for ^{12}CO and ^{13}CO, respectively. Typical root-mean-square (RMS) noise levels on spectra were 0.06 K at 115 GHz and 0.02 K at 110 GHz in antenna temperature scale. Antenna pointing was checked and corrected using circumstellar SiO ($J = 1 \rightarrow 0$) maser sources within $\sim$15° of each target every $\sim$1–2 h, resulting in an accuracy of $\lesssim$5 arcsec.

The integration time has been set to achieve an RMS noise level of $\sim$0.01 K. We have observed CO ($J = 1 \rightarrow 0$) emission towards 208 stars and detected the ^{12}CO and ^{13}CO emission in 96 and 34 stars, respectively. The data were reduced with JAVANEWSTAR[2] software. After the date were integrated in time domain, spectral baseline fitting was applied. Results of the single-point observations are summarized in A1. However, this paper focuses on spatial distributions in CO ($J = 1 \rightarrow 0$) emission, and therefore detailed results and statistical discussion with the full data set of the single-point observations will be presented in a future paper.

2.3 Mapping observations

Mapping observations have been conducted for 42 stars, including 34 brightest stars in ^{13}CO ($J = 1 \rightarrow 0$) emission from the single-point observations and 8 brightest stars in the NESS–JCMT observations (P. Scicluna et al. 2022). We have conducted the mapping observations with on-the-fly (OTF) mode using the NRO 45 m telescope and the FOREST receiver. Integration time has been set to achieve an RMS noise level of $\sim$0.1 K in main-beam temperature $T_{\rm mb}$ scale.

Receiver, spectrometer, and parameters were the same as those used for the single-point observations. Typical RMS noise levels were 0.1 and 0.07 K at 115 and 110 GHz, respectively, on maps. The mapping observations covered a map size of 170 arcsec × 170 arcsec centred on each target with a scan separation of 5 arcsec. Antenna pointing was checked and corrected using circumstellar SiO ($J = 1 \rightarrow 0$) maser sources within $\simeq$ 15° of the targets every $\sim$ 1–2 h, resulting in an accuracy of $\lesssim$ 5 arcsec. Occasionally, strong winds caused pointing offsets, which may artificially elongate observed envelopes along the wind direction. In such cases, the elongation would consistently appear in the same direction across all velocity-channel maps, allowing us to distinguish wind–induced artifacts from intrinsic structures.

Flux calibration source for daily fluctuations in antenna temperature was observed in only December 2021–February 2022 semester, but not in the other semesters. Therefore, the daily fluctuations in the other semesters was not calibrated. However, the daily fluctuations obtained from the observation using FOREST is $\sim$ 20 per cent of peak intensity, and mass-loss rate is not affected by the antenna temperature significantly ($\dot{M} \propto T_{\rm mb}^{5/6}$ shown later). Therefore, uncertainties of the mass-loss rates due to the non-calibration is likely less than an order of magnitude. In addition, this uncertainty does not impact CSE morphology or radial profiles.

The mapping data were processed with NOSTAR[3] software. After a linear baseline was subtracted from each raw spectral profile, the data were stacked into 5 arcsec grids using a spheroidal function to make image cubes for both X and Y scans. Then, a basket-weaving technique (D. T. Emerson & R. Graeve 1988) was employed to remove scanning effect. Finally, the X and Y image cubes were combined.

3 RESULTS

Out of 42 mapped stars, we detected ^{12}CO emission in 23 stars and ^{13}CO emission in 14 stars. Although all 42 stars were detected with bright ^{12}CO emission in the single-point observations, 19 were classified as non-detections in the mapping observations. In some of these 19 stars, detected emission on the maps was dominated by molecular clouds rather than by CSEs. Therefore, even though ^{12}CO emission was detected on the maps, we did not regard such stars as detections. In addition, the sensitivity of the mapping observations was insufficient for recovering the CO emission detected in the single-point observations due to difficulty of achieving sufficient integration time at each position on the maps using the OTF mode in mapping observations, compared to the single-point observations. In contrast, U Ori is also classified as non-detection because another CO emission source was observed at off-point, possibly cancelling the emission toward on-point. The results are summarized in Table 1. Fig. 1 shows velocity-integrated maps for the 23 stars for which CO emission from the CSEs was detected. Grey thick and black thin contours present the velocity-integrated brightness distributions of ^{12}CO and ^{13}CO emission, respectively. These maps were made by integrating along velocity channels after masking grids with fainter brightness than 3σ in each channel.

Table 3 summarizes angular sizes of observed CSEs in ^{12}CO and ^{13}CO ($J = 1 \rightarrow 0$) emission. For most stars, the CSE sizes were derived from two-dimensional elliptical Gaussian fitting. However, for SV Peg, its CSE size was derived from simple elliptical fitting, because the CSE shows an extended structure to the south from the brightest region, making it difficult for a Gaussian model to adequately represent the observed asymmetry. The measured CSE sizes reveal systematic differences between ^{12}CO and ^{13}CO. ^{12}CO envelopes are consistently larger than ^{13}CO envelopes. Using mean diameters based on the fitting results, the mean size ratios of ^{12}CO to ^{13}CO and standard deviations are $\sim$ 1.4 ± 0.2 for O-rich stars, 1.5 ± 0.5 for C-rich stars, and 2.5 ± 0.6 for S stars.

In several stars, the fitted CSEs deviate from circular symmetry. A more detailed discussion of the CSE morphologies is presented in Section 4.3.

3.1 CO line profile and mass-loss rate

Fig. 2 shows normalized spectra of the 23 stars, which were obtained by integrating CO emission over the entire CSEs. Thick grey and black dashed lines present spectral profiles of ^{12}CO and ^{13}CO emission, respectively. Table 2 shows parameters of the observed stars: name, distance (D) and its error (D err) in units of parsec, terminal velocity (V_∞) and its error (V_∞ err) in units of km s^{-1}, systemic velocity ($V_{\rm sys}$) in units of km s^{-1}, and peak flux density of the CO emission and RMS noise level in units of Kelvin, mass-loss rate ($\dot{M}$) and its uncertainty in unit of M$_\odot$ yr^{-1}. These parameters are derived from the CO line profiles in Fig. 2. The $V_{\rm sys}$ and V_∞ are centre velocity and half-width of the CO emission higher than 3σ,

[2] https://www.nro.nao.ac.jp/~nro45mrt/html/obs/newstar/

[3] https://www.nro.nao.ac.jp/~nro45mrt/html/obs/otf/reduction_en.html

Table 1. Spectral properties of observed stars.

IRAS PSC ID	Target	R.A. (J2000)	Dec. (J2000)	$T_{\rm mb^{12}CO}$ (K)	$\sigma_{^{12}CO}$ (K)	$T_{\rm mb^{13}CO}$ (K)	$\sigma_{^{13}CO}$ (K)	^{12}CO contour level (%)	^{13}CO contour level (%)
(1)	(2)	(3)	(4)	(5)	(6)	(7)	(8)	(9)	(10)
O-rich star									
02469+5646	W Per	02 50 37.9	+56 59 00	–	0.36	–	0.20	–	–
01037+1219	WX Psc	01 06 26.0	+12 35 53	1.13	0.04	0.12	0.03	(1, 20, 45, 75, 95)	(10, 50, 80, 95)
02168−0312	*o* Cet	02 19 20.8	−02 58 40	4.53	0.11	0.49	0.05	(10, 20, 40, 80, 95)	(20, 40, 80, 95)
03507+1115	IK Tau	03 53 28.9	+11 24 22	2.37	0.11	0.27	0.05	(10, 30, 60, 95)	(10, 40, 80, 95)
04566+5606	TX Cam	05 00 51.2	+56 10 54	1.16	0.14	–	0.06	(10, 50, 90)	–
05377+3548	IRAS 05377+3548	05 41 08.5	+35 49 55	–	0.07	–	0.04	–	–
05411+6957	BX Cam	05 46 44.3	+69 58 24	1.34	0.07	–	(0.03	10, 40, 80, 95)	–
05528+2010	U Ori	05 55 49.2	+20 10 31	–	0.15	–	0.07	–	–
08003+3629	SV Lyn	08 03 39.9	+36 20 42	–	0.09	–	0.06	–	–
09429−2148	IW Hya	09 45 15.2	−22 01 45	0.72	0.11	0.14	0.06	(10, 40, 80, 95)	(45, 75, 90)
09448+1139	R Leo	09 47 33.5	+11 25 44	0.44	0.09	–	0.06	(10,50, 90)	–
10580−1803	R Crt	11 00 33.9	−18 19 30	0.65	0.15	–	0.09	(10, 50, 85)	–
13114−0232	SW Vir	13 14 04.4	−02 48 25	0.71	0.11	–	0.03	(10, 40, 70, 95)	–
14219+2555	RX Boo	14 24 11.6	+25 42 13	0.75	0.07	0.10	0.04	(10, 50, 80, 95)	(50, 80)
15492+4837	ST Her	15 50 46.6	+48 28 59	0.33	0.10	–	0.06	(10, 35, 80)	–
18155−1206	IRAS 18155–1206	18 18 21.5	−12 05 21	–	0.36	–	0.17	–	–
18303−0519	IRAS18303-0519	18 33 01.0	−05 17 20	–	0.72	–	0.32	–	–
18535+0726	OH 40.1+2.4	18 55 57.0	+07 30 30	–	0.38	–	0.24	–	–
18595+0107	IRAS 18595+0107	19 02 02.7	+01 11 42	–	0.63	–	0.29	–	–
19597+3327A	2MASX J20013735+3335282	20 01 37.4	+33 35 28	–	0.17	–	0.14	–	–
20002+3322	IRAS 20002+3322	20 02 13.6	+33 31 20	–	0.21	–	0.10	–	–
20077−0625	V1300 Aql	20 10 27.9	−06 16 14	1.56	0.08	0.45	0.02	(1, 20, 45, 75, 95)	(30, 45, 69, 95)
20502+4709	RZ Cyg	20 51 53.2	+47 21 20	–	0.14	–	0.06	–	–
22035+3506	SV Peg	22 05 42.1	+35 20 55	1.24	0.05	–	0.03	(1, 15, 55, 90)	–
22177+5936	NSV 25 875	22 19 27.5	+59 51 22	–	0.46	–	0.24	–	–
23558+5106	R Cas	23 58 24.9	+51 23 20	0.85	0.26	–	0.11	(10, 30, 60, 90)	–
C-rich star									
04395+3601	RAFGL 618	04 42 53.6	+36 06 53	2.21	0.06	0.69	0.03	(1, 20, 45, 75, 95)	(10, 50, 80, 95)
05388−0147	IRAS 05388–0147	05 41 23.6	−01 46 00	–	0.17	–	0.07	–	–
09116−2439	CQ Pyx	09 13 53.9	−24 51 25	2.25	0.13	0.18	0.07	(10, 30, 60, 95)	(20, 50, 90)
09452+1330	CW Leo	09 47 57.4	+13 16 44	16.82	0.17	2.71	0.06	(1,5,10,20,40, 80, 95)	(1,5,10, 20, 40, 70, 95)
10131+3049	RW LMi	10 16 02.3	+30 34 19	4.68	0.08	0.47	0.05	(10, 30, 60, 95)	(10, 40, 80, 95)
10491−2059	V Hya	10 51 37.3	−21 15 00	2.60	0.18	–	0.07	(10,30, 60, 90)	–
12427+4542	Y CVn	12 45 07.8	+45 26 25	0.61	0.10	0.39	0.05	(10, 40, 80, 95)	(10, 40, 70, 90)
17441−2411	RAFGL 5385	17 47 13.5	−24 12 51	–	0.14	–	0.04	–	–
23320+4316	LP And	23 34 27.5	+43 33 01	2.30	0.07	0.73	0.04	(1, 15, 55, 90)	(1, 20, 45, 75, 95)
S star									
19126−0708	W Aql	19 15 23.4	−07 02 50	3.16	0.14	0.20	0.08	(10, 30, 60, 90)	(30, 60, 90)
19486+3247	χ Cyg	19 50 33.9	+32 54 51	3.44	0.08	0.14	0.01	(10, 30, 60, 95)	(10, 50, 80)
unknown									
18162−0246	RAFGL 5466	18 18 50.1	−02 45 29	–	0.73	–	0.30	–	–
22133+5837	V653 Cep	22 15 07.3	+58 52 47	–	0.42	–	0.29	–	–
22544+6141	IRAS 22544+6141	22 56 26.5	+61 57 34	–	0.49	–	0.28	–	–
22548+6147	IRAS 22548+6147	22 56 51.5	+62 03 43	–	0.42	–	0.22	–	–
22540+6146	2MASX J22560350+6202554	22 56 03.5	+62 02 55	–	0.49	–	0.25	–	–

Note. The columns list (1) IRAS PSC ID, (2) target name, (3) Right Ascension, (4) Declination, (5) peak main-beam temperature on the maps in ^{12}CO emission, (6) root-mean square (RMS) noise level for ^{12}CO emission at 115 GHz, (7) peak main-beam temperature on the maps in ^{13}CO emission, (8) RMS noise level for ^{13}CO emission at 110 GHz, (9) contour levels in percentage of the peak value in ^{12}CO maps shown in Fig. 1 and (10) contour levels in percentage of the peak value in ^{13}CO maps shown in Fig. 1. Non-(or Negative) detections are represented by dots.

respectively. The error in V_∞ is defined as the difference between V_∞ derived from emission higher than 3σ and 5σ.

The mass-loss rate in units of $M_\odot$ yr^{-1} is derived from

$$\dot{M} = 4.55 \times 10^{-19} \left(\frac{T_{\rm mb}}{\log(1/0.04)} \right)^{\frac{5}{6}} \times f_{\rm co}^{-1} V_\infty^{11/6} (DB)^{5/3} \qquad (1)$$

(G. R. Knapp & M. Morris 1985; H. Olofsson et al. 1993; M. A. T. Groenewegen et al. 1999; H. Imai et al. 2009). Here, $T_{\rm mb}$ is main beam temperature of ^{12}CO emission in units of Kelvin, V_∞ the terminal velocity in units of km s^{-1}, D the star distance in units of parsec, and B the beam size of telescope in units of arcsecond, $f_{\rm co}$ the abundance of CO molecule relative to H_2. $f_{\rm co}$ is assumed to be 1.0×10^{-3} for C-rich, 6.0×10^{-4} for S stars, and 2.0×10^{-4} for O-rich stars (S. Ramstedt et al. 2008). This equation is derived from radiative transfer modelling of CO line emission in CSEs by G. R. Knapp & M. Morris (1985), specifically from their equations (6) and (8). It is based on physical assumptions including spherical symmetry, steady mass-loss, constant expansion velocity, a fixed CO abundance relative to H_2, and optically thin envelope. Deviations from these assumptions, such as optically thick envelope, clumpy or asymmetric structures, or time variable mass-loss, can introduce systematic uncertainties. In Table 2, uncertainties were calculated by propagating the measurement errors in $T_{\rm mb}$, V_∞, and D, assuming the model itself is exact. Therefore, true uncertainties in the mass-loss rate are likely larger than the reported values in the Table 2.

The $\dot{M}$ equation has been applied for a data of a single-point observation in which a whole envelope is within beam size. However, our mapping observations have resolved CSEs as shown in Fig. 1. Therefore, Table 2 lists CO spectral parameters integrated over entire spatial extent of each CSE, so that the values represent the total emission from each CSE.

For CW Leo, its mass-loss rate is probably underestimated because its envelope is larger than the map size, leading to underestimate CO emission integrated over entire envelope. Instead, a lower limit to the mass-loss rate was calculated.

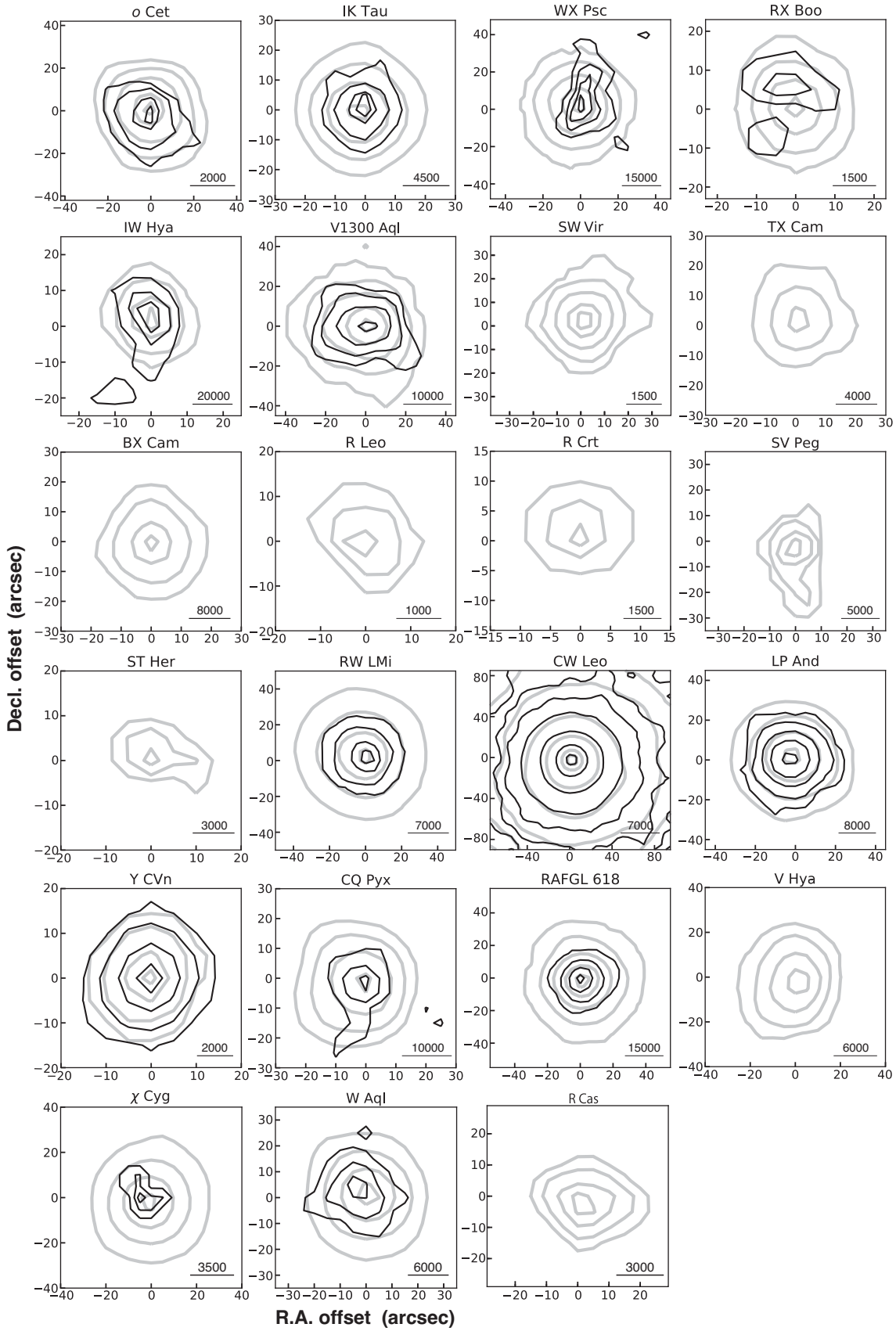

Figure 1. Integrated intensity maps in ^{12}CO (grey contours) and ^{13}CO (black contours) emission. The numbers at bottom right corners on each map are actual sizes in unit of au derived from distances shown in Table 2. NRO beam size is $\sim$15 $''$. The contour levels for each source are mentioned in Table 1.

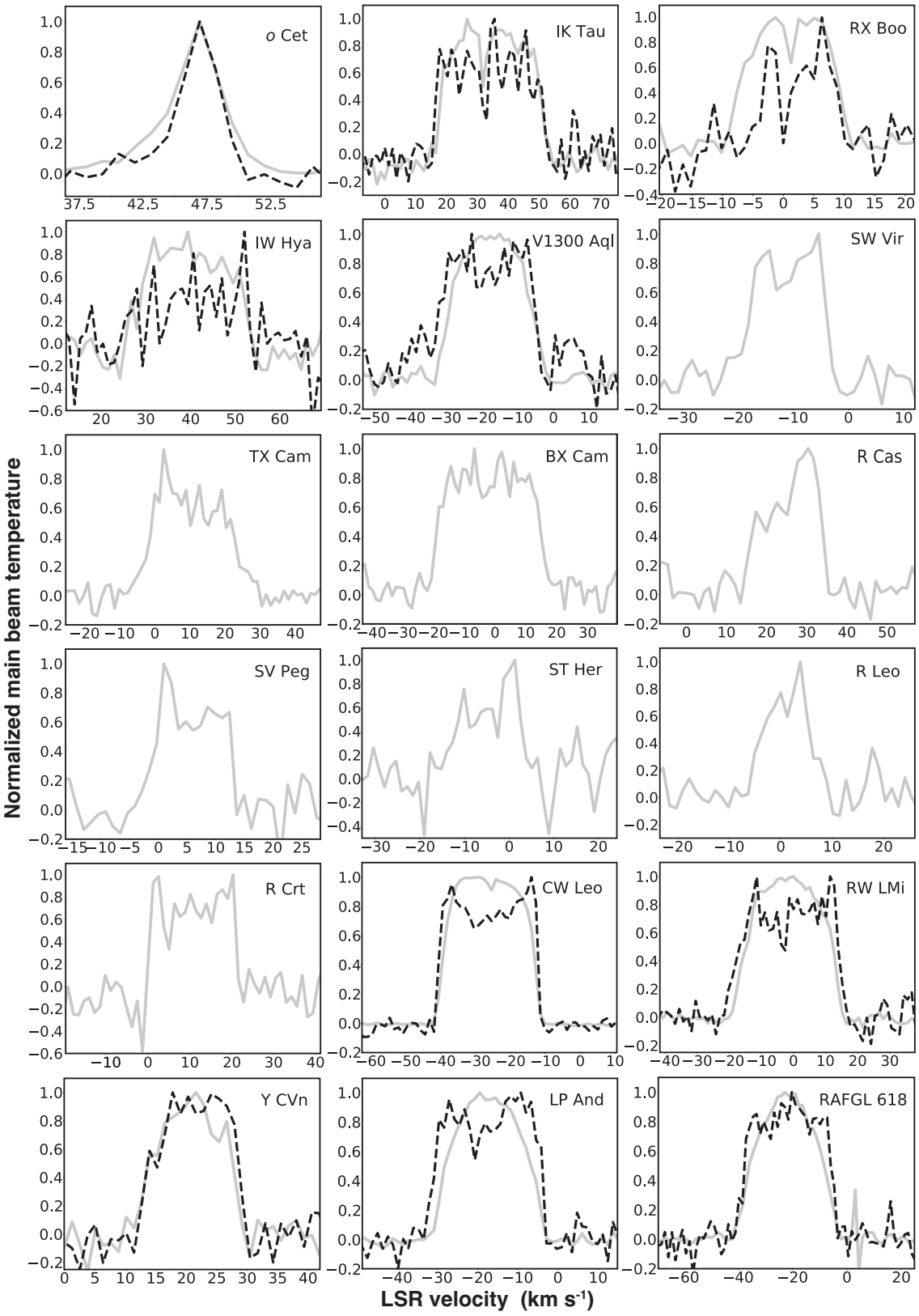

Figure 2. Normalized spectra integrated over the entire envelope for the 23 stars detected in CO emission. Gray solid and black dashed lines show spectra of ^{12}CO and ^{13}CO emission, respectively. Each target name is displayed on upper right sides of each spectrum. The line-of-sight velocity is given with respect to the local standard of rest.

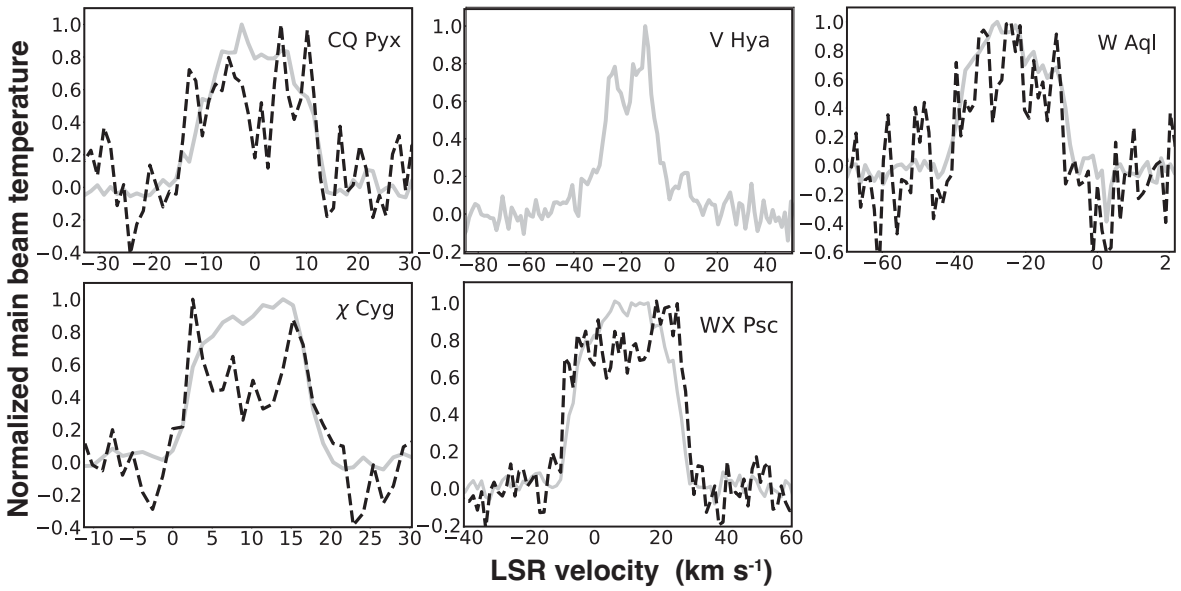

Figure 2. continued.

Table 2. Physical parameters derived from CO spectra.

Star	D (pc)	V_∞ (km s^{-1})	V_∞ err (km s^{-1})	V_{sys} (km s^{-1})	^{12}CO peak (K)	$\sigma_{^{12}CO}$ (K)	$\dot{M}$ (10^{-7} M$_\odot$ yr^{-1})	$\sigma_{\dot{M}}$ (10^{-7} M$_\odot$ yr^{-1})
(1)	(2)	(3)	(4)	(5)	(6)	(7)	(8)	(9)
O-rich star								
WX Psc	720^{+30}_{-30} [a]	18.4	0.0	9.2	86.75	3.20	7.8×10^2	$^{+5.9}_{-5.9} \times 10^1$
o Cet	92^{+12}_{-9} [b]	5.7	1.3	45.1	189.67	4.29	5.7	$^{+2.7}_{-2.5}$
IK Tau	289^{+54}_{-88} [a]	16.5	1.3	34.3	79.16	8.66	1.3×10^2	$^{+4.6}_{-6.9} \times 10^1$
TX Cam	292^{+35}_{-47} [a]	12.1	1.3	10.8	64.55	4.54	6.3×10^1	$^{+1.8}_{-2.1} \times 10^1$
BX Cam	579^{+10}_{-10} [a]	17.1	1.3	−2.2	25.73	2.77	1.70×10^2	$^{+2.9}_{-2.9} \times 10^1$
IW Hya	1794^{+755}_{-464} [d]	12.7	2.5	39.4	16.18	2.01	4.50×10^2	$^{+3.6}_{-2.6} \times 10^2$
R Leo	100^{+5}_{-5} [a]	3.8	1.3	−0.7	11.00	1.37	2.9×10^{-1}	$^{+1.8}_{-1.8} \times 10^{-1}$
R Crt	237^{+40}_{-64} [a]	9.5	0.0	10.8	12.89	2.08	7.4	$^{+2.3}_{-3.5}$
SW Vir	125^{+16}_{-12} [a]	7.0	0.6	−11.1	58.78	4.45	5.2	$^{+1.4}_{-1.2}$
RX Boo	139^{+9}_{-11} [a]	8.3	0.0	0.6	26.70	2.15	4.4	$^{+5.6}_{-6.5} \times 10^{-1}$
ST Her	324^{+57}_{-86} [a]	5.7	5.1	−4.5	4.95	0.87	2.2	$^{+3.7}_{-3.8}$
V1300 Aql	431^{+108}_{-108} [c]	14.3	1.3	−17.7	81.81	3.93	2.0×10^2	$^{+9.0}_{-9.0} \times 10^1$
SV Peg	334^{+7}_{-7} [a]	6.3	0.6	6.0	6.70	0.86	3.6	$^{+7.5}_{-7.5} \times 10^{-1}$
R Cas	200^{+10}_{-2} [a]	9.1	1.3	25.1	60.23	6.18	1.9×10^1	$^{+5.4}_{-5.2}$
C-rich star								
RAFGL 618	638^{+159}_{-159} [c]	18.8	0.0	−22.2	220.54	3.59	3.9×10^2	$^{+1.6}_{-1.6} \times 10^2$
CQ Pyx	604^{+151}_{-151} [c]	13.3	1.9	−0.6	98.58	5.38	7.1×10^1	$^{+3.5}_{-3.5} \times 10^1$
CW Leo	190^{+20}_{-20} [a]	14.6	0.0	−26.0	3592.76	26.11	2.5×10^2	$^{+4.3}_{-4.3} \times 10^1$
RW LMi	319^{+22}_{-27} [a]	15.9	0.0	−1.9	397.07	9.12	1.1×10^2	$^{+1.3}_{-1.6} \times 10^1$
V Hya	311^{+35}_{-36} [a]	24.1	10.8	−16.51	122.72	6.20	8.4×10^1	$^{+7.1}_{-7.1} \times 10^1$
Y CVn	249^{+22}_{-25} [a]	7.0	0.6	20.9	12.79	1.22	9.2×10^{-1}	$^{+2.1}_{-2.2} \times 10^{-1}$
LP And	428^{+40}_{-50} [a]	12.7	0.0	−16.8	247.11	6.86	8.0×10^1	$^{+1.3}_{-1.6} \times 10^1$
S star								
W Aql	380^{+49}_{-68} [a]	15.2	0.0	−24.1	148.72	8.12	9.9×10^1	$^{+2.2}_{-3.0} \times 10^1$
χ Cyg	180^{+10}_{-5} [a]	8.3	1.3	9.5	138.92	9.08	8.9	$^{+2.7}_{-2.6}$

Notes. The different columns list (1) target name, (2) distance and its uncertainty, (3) terminal line-of-sight velocity with respect to the local standard of rest (LSR), (4) error of terminal line-of-sight velocity, (5) systemic line-of-sight velocity with respect to LSR, (6) peak flux density in ^{12}CO emission integrated over entire CSE, (7) RMS noise level for ^{12}CO spectra at 115 GHz, (8) mass-loss rate derived from equation (1) and (9) uncertainty of the mass-loss rate.
References: [a] – M. Andriantsaralaza et al. (2022), [b] – F. Leeuwen (2007), [c] – P. Scicluna et al. (2022), [d] – C. A. L. Bailer-Jones et al. (2021).

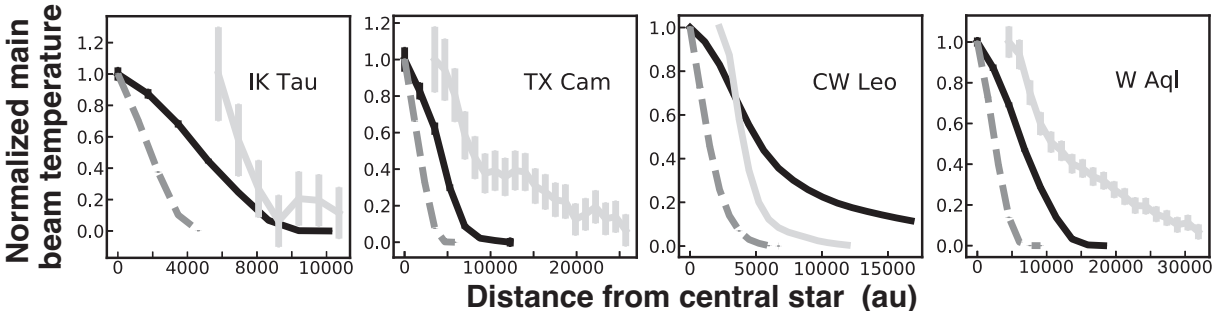

Figure 3. Radial profiles of normalized main-beam temperature in CO [$J = 3 \rightarrow 2$ (dark grey, dashed line) and $1 \rightarrow 0$ (black solid line)] emission lines and in 870 μm dust continuum (light grey, solid line) for stars observed with both the NRO and the JCMT in the NESS project. Error bars are shown in the dust continuum profile in CW Leo and in the CO emission profiles, but their intensities are so large that the error bars are very small. Although these radial profiles were not deconvolved with the telescope beam, the envelopes are larger than the beam size and were spatially resolved with the beam. In fact, the beam size is 15 arcsec, while the data point separation of the radial profiles in CO ($J = 1 \rightarrow 0$) emission is 5 arcsec. The dust continuum profiles do not extend to the centre as the ^{12}CO emission profiles because the strong continuum emission from the central star and dust at the centre of the envelopes was subtracted, which makes it easier to consider the extended envelopes.

3.2 Comparison of radial profiles of the brightness distributions in CO and 850 μm continuum emission

To compare the CSE sizes in CO ($J = 1 \rightarrow 0$) emission with those in CO ($J = 3 \rightarrow 2$) and 870 μm dust continuum, we examined their radial profiles of normalized main-beam temperature, as shown in Fig. 3. The radial profiles were obtained by calculating average brightness of annulus at each radius from the centre to outer edge of the envelopes. The data of CO ($J = 3 \rightarrow 2$) emission and continuum were obtained by the NESS–JCMT observations (T. E. Dharmawardena et al. 2018; P. Scicluna et al. 2022). Particularly, for the continuum data, T. E. Dharmawardena et al. (2018) provides the radial profiles. The observed continuum emission from the central region of CSE includes contributions from not only hot, dense dust but also central star. Because the aim of this study is to reveal spatial extent of the CSEs, these inner components were subtracted. This subtraction made it easier to analyse extended dust continuum and allowed us to better assess CSE sizes of outer envelope. Details of this analysis are described in T. E. Dharmawardena et al. (2018).

Comparing the CSE sizes between CO ($J = 3 \rightarrow 2$) and CO ($1 \rightarrow 0$) emission based on the radial profiles not on the fitting results, the sizes of CO ($J = 1 \rightarrow 0$) envelopes are twice or more as large as that those of CO ($J = 3 \rightarrow 2$) envelopes in all stars. In contrast, the sizes in CO ($J = 1 \rightarrow 0$) and dust envelopes are not correlated. In CW Leo, CO ($J = 1 \rightarrow 0$) envelope is larger than dust envelope (gas envelope ($\gtrsim$ 17 000 au) > dust envelope (∼12500 au)). On the other hand, in TX Cam, CO ($J = 1 \rightarrow 0$) envelope is smaller than dust envelope [gas envelope (∼13 000 au) < dust envelope (∼25 000 au)] and W Aql [gas envelope (∼18 000 au) < dust envelope (∼31 000 au)]. Furthermore, in IK Tau, CO ($J = 1 \rightarrow 0$) and dust envelope are almost equal in size [gas envelope ∼ dust envelope (∼10 000 au).

3.3 Radial profiles in CO-isotope ratio, ^{12}CO and ^{13}CO ($J = 1 \rightarrow 0$), and ^{12}CO optical depth

Fig. 4 shows radial profiles of ^{12}CO/^{13}CO intensity ratio for 14 stars detected in both ^{12}CO and ^{13}CO emission on the maps. In many envelopes, larger errors in outer regions caused by weak ^{13}CO intensity. In fact, in normalized radial profiles of ^{12}CO and ^{13}CO emission in Fig. 5, ^{13}CO intensity is significantly weaker than ^{12}CO intensity in the outer regions. Large errors in ^{13}CO intensity in Fig. 5 are caused by low signal-to-noise ratio.

In 9 out of 14 stars (IK Tau, WX Psc, V1300 Aql, CW Leo, RW LMi, RAFGL 618, LP And, CQ Pyx, and χ Cyg), the ^{12}CO/^{13}CO intensity ratios increase outward from the centre of envelopes. Except for CW Leo, these increases in the ratios are not due to increases in ^{12}CO intensity, but due to decrease in ^{13}CO intensity relative to ^{12}CO intensity to outer envelope as shown in Fig. 5.

If the observed envelopes is optically thick, the radial profiles does not reliably reflect that of CO column density. In order to evaluate this optical depth effect, we estimated optical depths of the CSEs by solving radiative transfer with numerical simulations using a toy model of CSE.

To obtain optical depths of the CSEs, we used the RADEX code, which calculates intensity of molecular (or atomic) emission lines by solving radiative transfer equation based on non-LTE analysis with the Large Velocity Gradient (LVG) approximation (F. F. S. der Tak et al. 2007). RADEX assumes a one-zone model that requires input parameters such as kinetic temperature, line width, and densities of H_2 and CO. However, since these parameters vary significantly with radius from the central star, we did not treat a CSE as a single zone. Instead, we first constructed a fine-grid CSE model with a smaller cell size than the observed map grid size, and then regrided this model into a coarser CSE model with the same cell size as the observed map grid size. In this coarser CSE model, the density and temperature were defined as the averages over the fine cells within each coarser cell, while the line width was determined from thermal and turbulent components together with a difference in line-of-sight velocity between the fastest and slowest fine-cells within each coarser cell.

The RADEX code calculated intensity from one cell, and then this intensity was used as an incident intensity to next cell along line-of-sight direction. This process was iterated for all cells along line-of-sight direction, and then the intensity from the final cell closest to observer was compared with the observed intensity. In particular, we simulated intensity at the centre of envelope to derive optical depth integrated along line of sight through the centre of the envelope.

At each cell, the kinetic temperature in units of Kelvin was calculated with the following equation,

$$T_{\rm k}(r) = T_{\rm star} \left(\frac{R_{\rm star}}{r} \right)^{\frac{2}{5}}, \quad (2)$$

where r is the distance from the central star in units of au (H. J. Habing & H. Olofsson 2003). $T_{\rm star}$ is the surface temperature of the

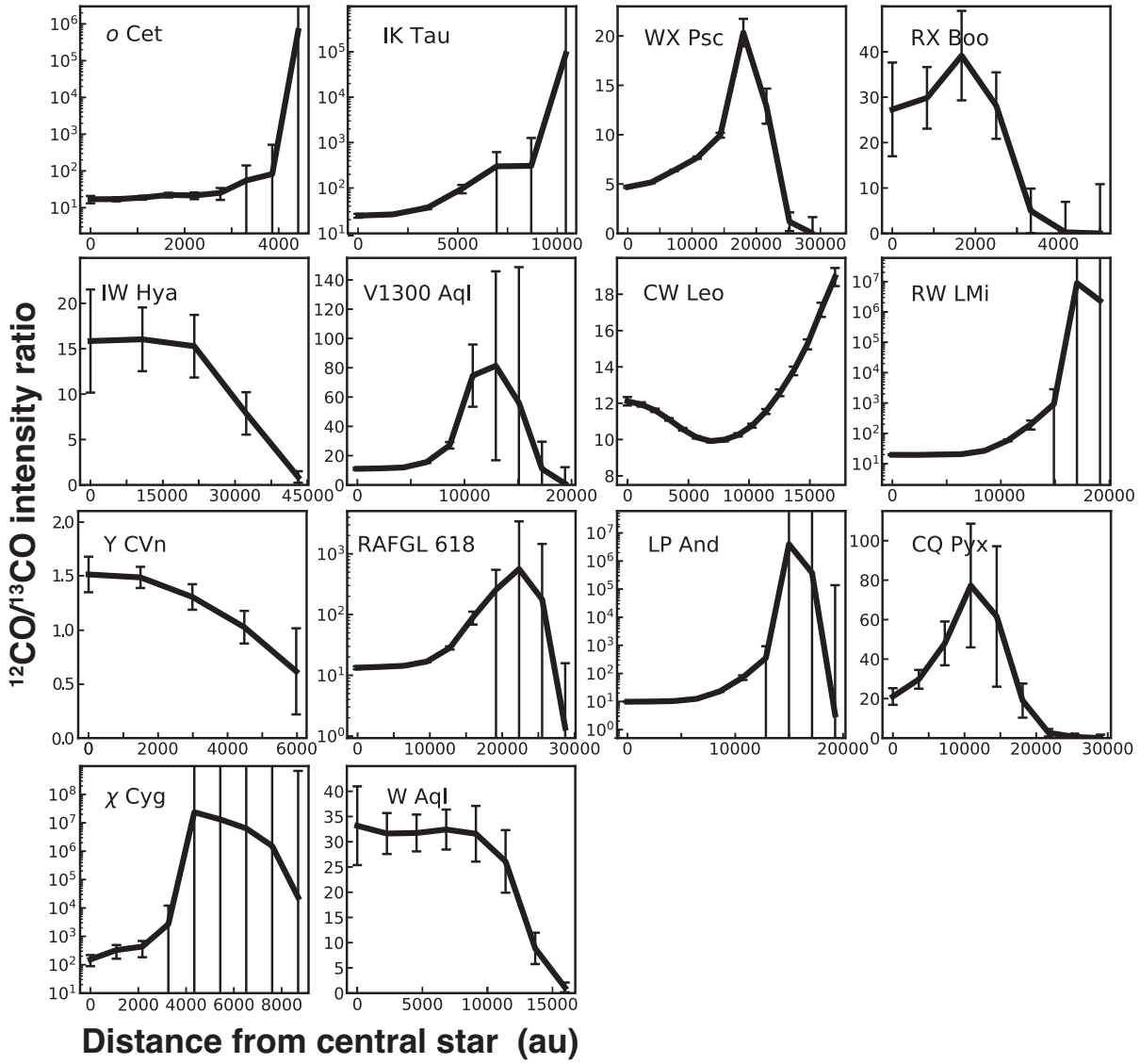

Figure 4. Radial profiles of ^{12}CO/^{13}CO intensity ratio. The larger errors in outer envelopes caused by weak ^{13}CO intensity. In 9 out of 14 stars (IK Tau, WX Psc, V1300 Aql, CW Leo, RW LMi, RAFGL 618, LP And, CQ Pyx, and χ Cyg), ^{12}CO/^{13}CO intensity ratios increase outward from the centre of envelopes. On the other hand, in three stars (IW Hya, W Aql, and Y CVn), ^{12}CO/^{13}CO intensity ratios simply decrease outward.

central star in units of Kelvin, which is assumed to be 2000 K for O-rich stars and 2400 K for C-rich stars and S stars (e.g. J. Bergeat, A. Knapik & B. Rutily 2001; A. M. Heras & S. Hony 2005; S. Ramstedt et al. 2008). $R_{\rm star}$ is the radius of the central star in unit of au, which we assume a typical value of 2 au (H. J. Habing & H. Olofsson 2004).

The line-width, Δv, is given by

$$\Delta v^2 = \Delta v^2_{\rm thermal} + \Delta v^2_{\rm turbulent} + \Delta v^2_{\rm expansion} \tag{3}$$

where $\Delta v_{\rm thermal}$ is the thermal line-width, $\Delta v_{\rm turbulent} = 3\,{\rm km\,s^{-1}}$ the turbulent velocity, and $\Delta v_{\rm expansion}$ the difference of radial expansion velocity between fastest and slowest gas in each cell. $\Delta v_{\rm thermal}$ is given in units of km s^{-1} by

$$\Delta v^2_{\rm thermal} = \frac{T_{\rm k}}{21.2(m_{\rm CO}/m_{\rm H})}, \tag{4}$$

where $T_{\rm k}$ is the kinetic temperature calculated in equation (2), and $m_{\rm CO}$ and $m_{\rm H}$ the masses of CO and atomic hydrogen, respectively (T. L. Wilson, K. Rohlfs & S. Hüttemeister 2013). $\Delta v_{\rm expansion}$ was calculated from the line-of-sight component of the expansion velocity given by

$$v_{\rm expansion}(r) = \sqrt{\frac{v^2_\infty \cdot r_\infty \cdot R_{\rm star}}{r_\infty - R_{\rm star}} \left(\frac{1}{r_\infty} - \frac{1}{r}\right) + v^2_\infty}, \tag{5}$$

where r_∞ is the radius of outer edge of CSE from the central star in units of au and V_∞ the terminal velocity. Equation (5) was derived from the equation of motion for dust receiving radiation pressure from the central star given by

$$\rho \frac{{\rm d}^2 r}{{\rm d}t^2} = \frac{L\kappa\rho}{4\pi c}\frac{1}{r^2}, \tag{6}$$

where L is the stellar luminosity, κ the absorption coefficient, ρ the gas density, c the speed of light. The r_∞ and V_∞ are given from our observations. Although the velocity calculated by equation (5) increases with r, the actual expansion velocity changes periodically in the vicinity of central star, affected by shock propagation generated by stellar pulsation. However, since the expansion velocity is almost

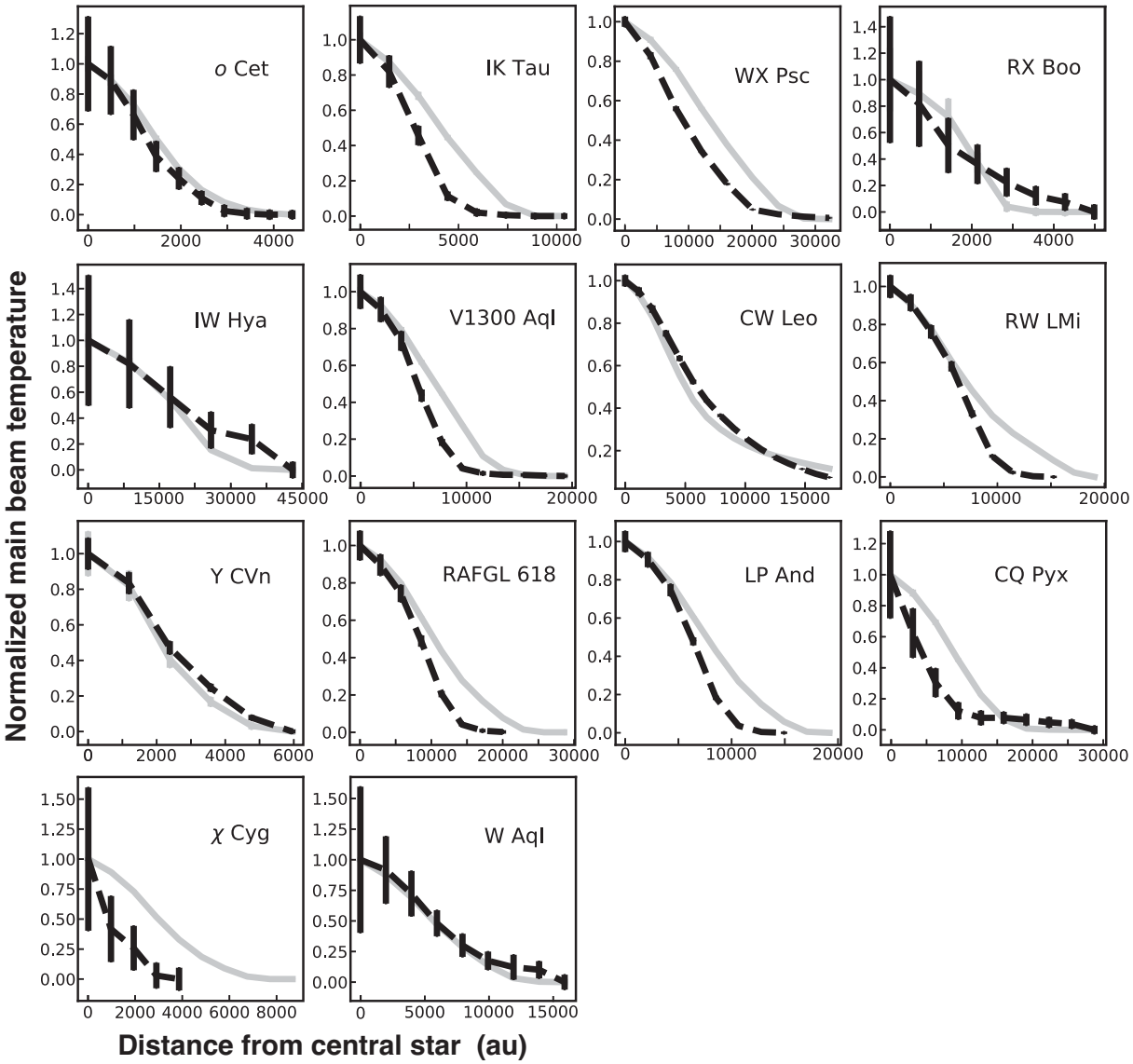

Figure 5. Radial profiles of normalized main-beam temperature in ^{12}CO (grey solid lines) and ^{13}CO ($J = 1 \rightarrow 0$) (black dashed lines) emission. Although these radial profiles were not deconvolved with the telescope beam, the envelopes are larger than the beam size and were spatially resolved with the beam. In fact, the beam size is 15″, while the data point separation of the radial profiles is 5″.

constant in most of envelope observed in CO emission, the velocity derived from equation (5) is used approximately in this simulation.

CO density was derived from H_2 density multiplied by f_{CO}. The H_2 density was given by

$$\rho(r) = \frac{\dot{M}}{4\pi r^2 v_{\rm expansion}(r)}, \tag{7}$$

where $\dot{M}$ is the mass-loss rate in units of $M_\odot$ yr^{-1}. By using $\dot{M}$ as an input parameter, we simulated optical depths.

Table 4 gives the results of our RADEX simulations for the observed stars in which both ^{12}CO and ^{13}CO emission lines were detected. The Table summarizes the simulated mass-loss rates and the optical depths integrated along the line of sight through the center of the envelopes. A comparison between the mass-loss rates estimated from the simulations and those derived from the observational data shows that several stars exhibit a ratio $\dot{M}_{\rm sim}/\dot{M}_{\rm obs} \geq 2$. Among these, stars for which the two values are consistent within the 3σ uncertainty range of the observational values cannot be regarded as statistically significant discrepancies. Specifically, CQ Pyx and RAFGL 618 are classified in this category. We therefore focus on CW Leo, *o* Cet, WX Psc, RW LMi, χ Cyg, and IK Tau, for which the discrepancies in the mass-loss rates are likely to be significant. The possible causes of these discrepancies, the reliability of the inferred optical depths, and the effects of optical depth on the detectability of thermal-pulse signatures are discussed in Section 4.3.

It should also be noted that the actual grid size in the toy model differs from star to star since it was adjusted to correspond to the observed map grid size in angular scale. Therefore, comparison of τ between different stars should be made with caution: a larger grid represents an average over a wider region, while a smaller grid can highlight localized regions. Nevertheless, this limitation does not critically affect our aim, which is to investigate whether thermal pulse signatures could be hidden due to optical depth.

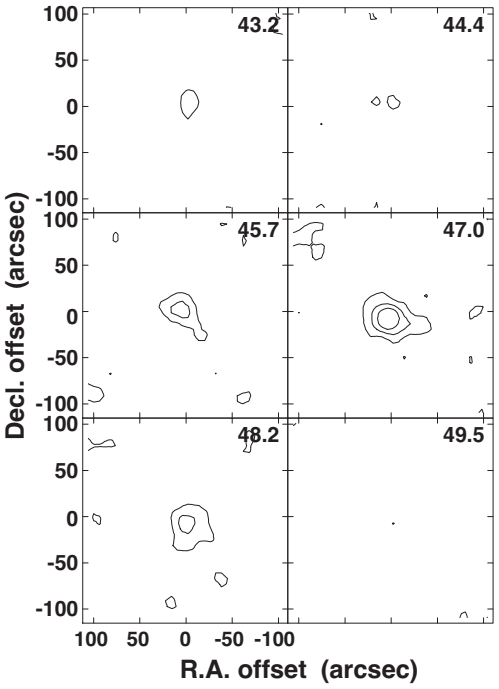

Figure 6. Channel maps of ^{13}CO ($J = 1 \rightarrow 0$) emission around *o* Cet. The number labels at upper right corners of each channel map shows the LSR velocity in units of km s^{-1}. The contour levels are $1\sigma \times (3,4,6)$, where $1\sigma = 0.11$ K.

3.4 Individual objects

We investigated envelope morphologies of all stars detected in CO emission, and some of envelopes exhibit aspherical morphologies, as shown in Fig. 1. However, several envelopes are likely to be due to strong wind affecting antenna pointing during OTF observations or low signal to noise ratio. Deviations from spherical symmetry of R Leo, R Cas, and V1300 Aql are similar for all channel maps, implying that they were caused by the misalignment of antenna pointing due to strong winds during OTF observations. In addition, aspherical envelopes of ST Her in ^{12} CO and IK Tau, RX Boo, IW Hya, CQ Pyx, χ Cyg, and W Aql in ^{13}CO were caused by low signal to noise ratio. However, in four stars (o Cet, WX Psc, SV Peg, and RAFGL 618), their aspherical morphologies are probably real because antenna pointing during the observation was good and asymmetric morphologies are found only in specific velocity channels.

In the velocity-integrated maps of *o* Cet in Fig. 1, the envelope in ^{12}CO emission has roughly spherical morphology, while that in ^{13}CO emission is elongated in the northeast–southwest direction. Fig. 6 shows channel maps in ^{13}CO emission, where the envelopes at 45.7 and 47.0 km s^{-1} is elongated in the south–west direction.

The velocity-integrated maps and channel maps of WX Psc (= IRC+10011) in ^{12}CO and ^{13}CO emission are shown in Figs 1, 7, and 8, respectively. The envelopes in ^{12}CO emission are spherical, while that in ^{13}CO emission is elongated in north-south direction.

Fig. 1 shows the velocity-integrated map of SV Peg, which exhibits elongation in the north–south direction. In channel maps shown in Fig. B1, the elongation is confirmed only at 0.9 and 2.2 km s^{-1}.

As shown in Fig. B2, the envelopes of RAFGL 618 are almost spherical in ^{12}CO emission. However, in ^{13}CO emission, the en-

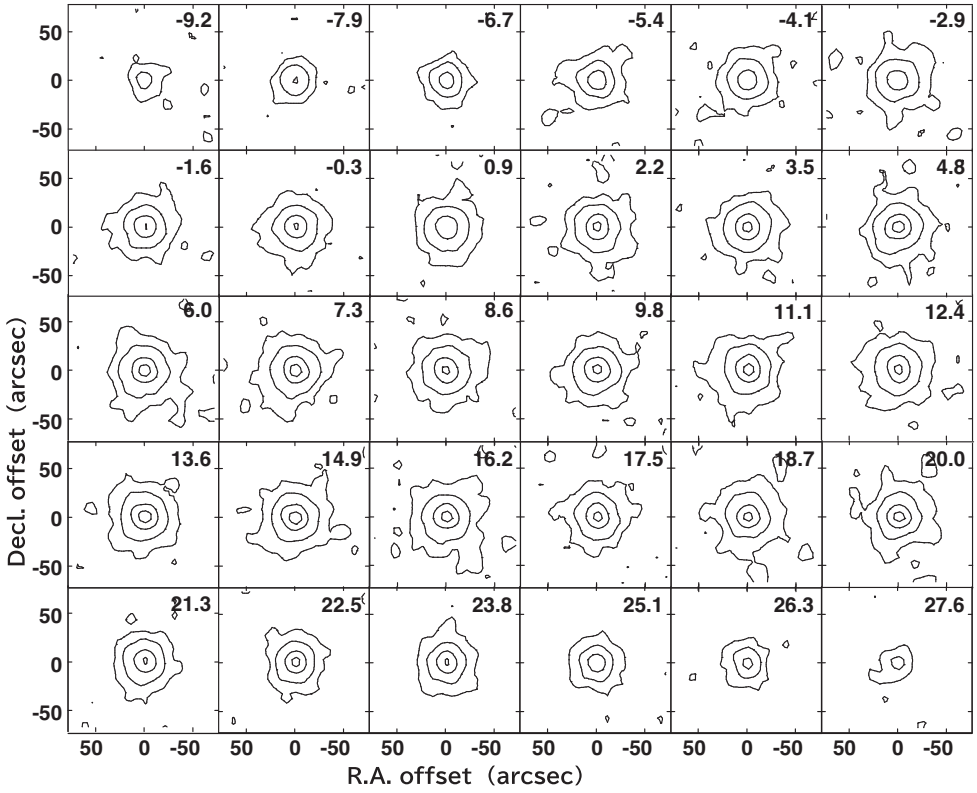

Figure 7. Channel maps of ^{12}CO ($J = 1 \rightarrow 0$) around WX Psc. The contour levels are $1\sigma \times (3, 10, 24, 35)$, where $1\ \sigma\ = 0.04$ K.

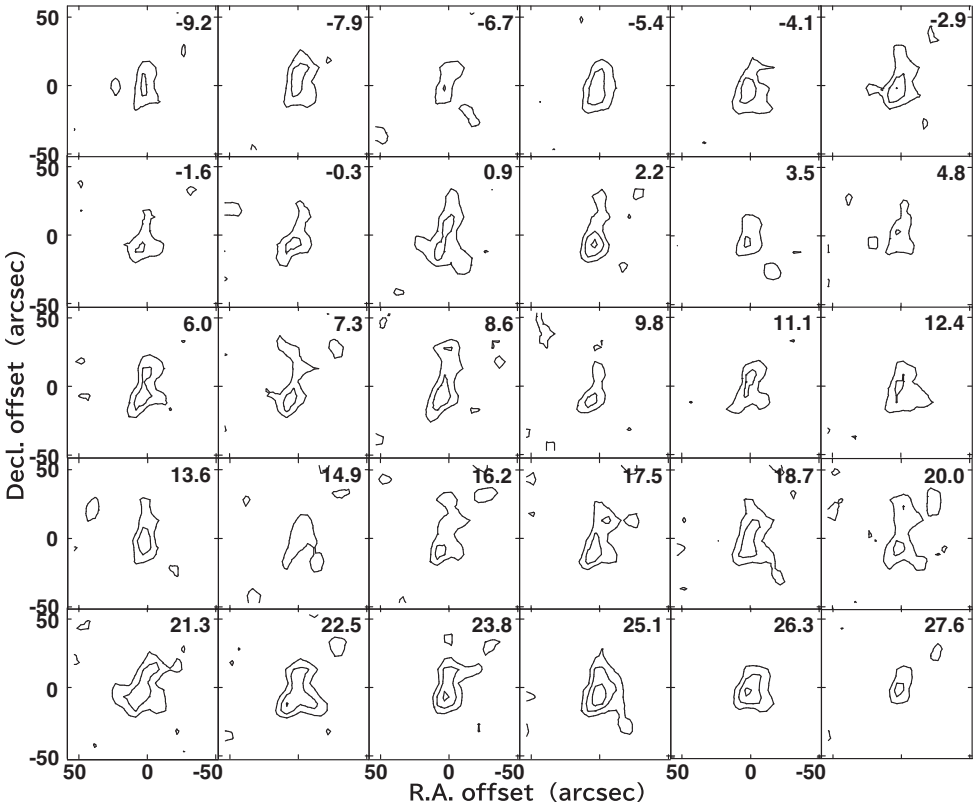

Figure 8. Channel maps of ^{13}CO ($J = 1 \rightarrow 0$) emission around WX Psc. The contour levels are $1\sigma \times (3, 4.5, 6)$, where $1\,\sigma\ = 0.03$ K.

velopes have aspherical morphology even at high signal-to-noise ratios ($> 5\sigma$) as shown in Fig. B3.

4 DISCUSSION

Single-dish observations in CO ($J = 1 \rightarrow 0$) emission are generally less effective for spatially resolving CSEs because of contamination from interstellar gas within a large beam. In contrast, interferometric observations typically have higher angular resolution but large scale structures are filtered out. However, our single-dish observations in CO ($J = 1 \rightarrow 0$) emission using NRO 45 m telescope mitigate these limitations thanks to their relatively small beam and high sensitivity, allowing us to trace more extended and colder components of CSEs than those probed by excited CO lines. As shown in Fig. 3, the CSEs detected in CO ($J = 1 \rightarrow 0$) emission appear to be twice or more extended than those in CO ($J = 3 \rightarrow 2$) emission to trace older mass-loss history.

The COSAS (CO Survey of late AGB Stars) project conducted mapping observations of representative AGB and post-AGB stars in CO ($J = 1 \rightarrow 0$) emission with the IRAM PdBI interferometry and IRAM 30 m single-dish telescopes (A. Castro-Carrizo et al. 2010). Although the COSAS survey reported CSE sizes measured down to a noise level (likely corresponding to 1σ) as shown in Table 4 in the paper, their published channel maps indicate that 3σ or 4σ contours trace more compact and reliably detected structures. On the other hand, our CSE sizes correspond to 3σ contour of CO ($J = 1 \rightarrow 0$) intensity distribution in the integrated intensity maps which were created using only grids with emission exceeding 3σ noise level. Therefore, for consistency in comparing the spatial extents of detected emission, we refer to the outermost contours corresponding to 3σ or 4σ noise level in the COSAS channel maps.

Table 3 also lists the CSE sizes obtained from the COSAS ^{12}CO($J = 1 \rightarrow 0$) data. For stars where both of the studies apply the 3σ detection threshold, our measured CSE sizes are only 5–10″ larger than those of COSAS. To compare sensitivities, the typical 1σ RMS noise in COSAS is 10–20 mJy beam^{-1} (A. Castro-Carrizo et al. 2010), whereas that of our observations is ∼0.10 K, corresponding to ∼240 mJy beam^{-1} when adopting a conversion factor of 2.4 Jy K^{-1} for $T_{\rm mb}$ with the NRO 45 m telescope at 115 GHz. Thus, our data are less sensitive, and the differences of CSE sizes cannot be attributed to a deeper detection of faint, extended emission in our maps. Since these envelopes are only moderately resolved by the 15″ beam of the NRO 45 m telescope, the determination of the outer CSEs boundaries is sensitive to beam convolution and the adopted edge criterion. Consequently, uncertainties in the measured outer radius can reach a few arcseconds up to approximately one beam. In addition, the outer CSEs boundaries in COSAS were determined visually, which introduces an additional uncertainty in the measured sizes. Therefore, the observed 5–10″ differences are consistent with the expected measurement uncertainty. For stars where the COSAS CSE sizes were measured at 4σ level, the COSAS envelopes would extend farther outward if evaluated with the same 3σ level as in this work, which would further reduce the apparent differences. We therefore conclude that the CSE sizes derived in our study are broadly consistent with the COSAS results, and that both of the datasets are probing essentially the same spatial extent of CO ($J = 1 \rightarrow 0$) envelopes.

Regarding size relation between CO and dust envelopes, there exists a variation among the stars. The detectable CSE size would depend on a sensitivity and/or circumstellar environment. Comparing the distances to the four stars shown in Fig. 3, the distances increase in following order CW Leo, IK Tau, W Aql, and TX Cam, and the

Table 3. CSE sizes in NESS–NRO and COSAS projets.

Star	^{12}CO ($J = 1 \rightarrow 0$)		^{13}CO ($J = 1 \rightarrow 0$)		COSAS
	CSE size (arcsec)	PA (deg)	CSE size (arcsec)	PA (deg)	CSE size (arcsec)
(1)	(2)	(3)	(4)	(5)	(6)
O-rich star					
WX Psc	62 × 60	7	57 × 23	−15	∼46 (4σ)
o Cet	92 × 83	40	69 × 55	52	
IK Tau	60 × 58	44	44 × 40	160	∼48 (4σ)
TX Cam	52 × 50	5	–	–	∼42 (3σ)
BX Cam	48 × 45	4	–	–	
IW Hya	41 × 36	21	35 × 22	12	
R Leo	40 × 31	44	–	–	
R Crt	27 × 22	92	–	–	
SW Vir	50 × 47	139	–	–	
RX Boo	51 × 46	22	39 × 37	77	∼44 (3σ)
ST Her	28 × 15	83	–	–	
V1300 Aql	69 × 59	73	61 × 50	75	
SV Peg	45 × 27†	184	–	–	
R Cas	49 × 36	80	–	–	∼42 (3σ)
C-rich star					
RAFGL 618	72 × 71	28	51 × 47	118	
CQ Pyx	63 × 60	6	28 × 24	174	
CW Leo	>170*	–	>170*	–	
RW LMi	106 × 101	48	72 × 70	54	
V Hya	82 × 68	163	–	–	
Y CVn	42 × 36	164	46 × 40	156	
LP And	70 × 65	76	54 × 52	92	
S star					
W Aql	73 × 70	31	41 × 33	100	
χ Cyg	77 × 74	161	36 × 16	29	∼48 (4σ)

Notes. The different columns list (1) target name, (2) angular CSE sizes derived from Gaussian fitting in ^{12}CO $J = 1 \rightarrow 0$ emission and are representative by [(major axis) × (minor axis)], (3) position angle of CSEs in ^{12}CO $J = 1 \rightarrow 0$ emission, (4) angular CSE sizes derived from Gaussian fitting in ^{13}CO $J = 1 \rightarrow 0$ emission, (5) position angle of CSEs in ^{13}CO $J = 1 \rightarrow 0$ emission, and (6) CSE sizes visually estimated from channel maps in ^{12}CO($J = 1 \rightarrow 0$) emission observed in COSAS project, with the values in parentheses indicating signal-to-noise ratios of the visually measured CSE sizes (A. Castro-Carrizo et al. 2010). The typical 1σ RMS noise level in COSAS channel maps is ∼10–20 mJy beam^{-1}. Non- (or negative) detection are representative by dots.
*: In CW Leo, because its CSE sizes are larger than map size (170 arcsec × 170 arcsec) of our observation, the CSE sizes and position angle could not be derived from fitting, and then are representative by >170 and hyphen, respectively.
†: For SV Peg, its CSE size was derived from simple elliptical fitting, instead of Gaussian fitting, because the CSE shows an extended structure to the south from the brightest region, making Gaussian fitting inadequate to measure its full extent.

size relations between the CO ($J = 1 \rightarrow 0$) gas envelope and dust envelope change according to this order. Therefore, the size relations may depend on the distance and the sensitivity. However, because CO ($J = 1 \rightarrow 0$) emission rapidly decreases along radial direction except for CW Leo as shown in Fig. 5, almost the entire envelopes in CO ($J = 1 \rightarrow 0$) emission would have been observed, and therefore increasing in the sensitivity would not change the observed CSE sizes. In fact, the CSE sizes in our study are consistent with the COSAS results.

Thus, the observed CSE sizes depend on circumstellar environment. CO molecules at the outer edge of CSE are photodissociated by UV radiation from interstellar medium (e.g. G. A. Mamon, A. E. Glassgold & P. J. Huggins 1988; M. Saberi, W. H. T. Vlemmings & E. De Beck 2019). As envelope expands, the gas density at the outer edge decreases and the CO molecules at the outer edge would be more easily photodissociated by the interstellar UV radiation. In Fig. 3, the CO ($J = 1 \rightarrow 0$) gas envelopes of TX Cam and W Aql extend to ∼13 000 au and ∼18 000 au, respectively, where CO molecules at the outer edge are likely to be photodissociated by interstellar UV radiation. By contract, the CO ($J = 1 \rightarrow 0$) gas envelope of IK Tau is ∼10 000 au, which is smaller than those of TX Cam and W Aql, suggesting that the CO molecules are not very actively photodissociated. Therefore, the size of the CO gas envelope is about equal to that of the dust envelope. However, in CW Leo, a C-rich star, the CO ($J = 1 \rightarrow 0$) gas envelope is $\gtrsim$17 000 au and larger than the dust envelope because the envelope is optically thick, making photodissociation less effective than in the other three stars. Dust grains mixed in the gas can also provide shielding against UV radiation and partly protect CO molecules from photodissociation. The role of dust shielding and its impact on the CO and dust envelope sizes are also discussed in the following section.

4.1 The cause of radial change of ^{12}CO/^{13}CO ratio

A ^{12}C/^{13}C abundance ratio is a probe of thermal pulse and third dredge up at the AGB phase. The ratio depends on initial mass as well as efficiency and iteration number of third dredge up. In the case of a 3 $M_{\odot}$ star, a photospheric ^{12}C/^{13}C ratio is predicted to be typically ∼20 before the AGB phase and to increase to ∼119 at

Table 4. Optical depth and mass-loss rate estimated with RADEX.

Target	$\dot{M}_{\rm sim}$ 10^{-7} ($M_\odot$ yr^{-1})	$\dot{M}_{\rm sim}/\dot{M}_{\rm obs}$	$\tau_{\rm sim}$	$CSE_{^{12}CO}/CSE_{^{13}CO}$
O-rich star				
WX Psc	3.1×10^2	0.4	0.06	1.5
o Cet	2.2×10^1	3.9	0.02	1.4
IK Tau	4.0×10^2	3.1	0.04	1.5
IW Hya	4.5×10^1	0.1	1.38	1.4
RX Boo	1.1×10^1	2.5	0.08	1.3
V1300 Aql	2.0×10^2	1.0	0.21	1.2
C-rich star				
RAFGL 618	7.4×10^1	0.19	0.33	1.5
CQ Pyx	1.8×10^1	0.25	2.05	2.4
CW Leo	1.4×10^3	5.6	2.60	
RW LMi	2.9×10^2	2.6	0.49	1.5
Y CVn	1.3	1.4	0.45	1.0
LP And	7.4×10^1	0.93	0.21	1.3
S star				
W Aql	1.4×10^2	1.4	0.21	1.9
χ Cyg	2.5×10^1	2.8	0.14	2.0

Note. Mass-loss rates ($\dot{M}$) and optical depths ($\tau_{\rm sim}$) estimated with RADEX for the observed stars in which both ^{12}CO and ^{13}CO emission were detected. The columns list the simulated mass-loss rate $\dot{M}_{\rm sim}$, the mass-loss rate ratio $\dot{M}_{\rm sim}/\dot{M}_{\rm obs}$, the simulated optical depth integrated along the direction of CSE centre$\tau_{\rm sim}$, and ^{12}CO/^{13}CO CSE size ratio derived from the observed CSE sizes.

the end of this phase (A. I. Karakas & J. C. Lattanzio 2014). In addition, ^{12}CO/^{13}CO be used as an tracer of the ^{12}C/^{13}C ratio. In our results, ^{12}CO/^{13}CO intensity ratios increase along radial direction in nine stars (IK Tau, WX Psc, V1300 Aql, CW Leo, RW LMi, RAFGL 618, LP And, CQ Pyx, and χ Cyg) even excluding the plot points with extremely large uncertainty as shown in Fig. 4, and the ^{12}CO/^{13}CO ratios increase to values in the range of ∼1–120. We note that the ^{12}CO/^{13}CO ratios shown in Fig. 4 are line intensity ratios, not abundance ratio. Because ^{12}CO emission is optically thick, the intensity ratio generally underestimates the underlying ^{12}CO/^{13}CO ratio. However, the optical depths estimated from our simulations in Table 4 are relatively small for most targets ($\tau_{\rm sim} \lesssim 0.5$), suggesting that the intensity ratios should not be strongly biased by the optical depth effects, as discussed in more detail in Section 4.3.

If the radial increase in the ^{12}CO/^{13}CO intensity ratio were caused by a past thermal pulse and third dredge-up, an associated enhancement in ^{12}CO column density would be expected at the same radius. This should produce a noticeable enhancement in ^{12}CO emission at the corresponding radius. In fact, previous studies have reported that detached shells with strong ^{12}CO emission appear at radius of a few 10^3–10^4 au (e.g. M. Maercker et al. 2024). Although our observations reach similar spatial scales, the radial profiles in Fig. 5 do not show such features. Instead, ^{12}CO emission smoothly declines outward. These results indicate that the radial changes of ^{12}CO/^{13}CO ratio are unlikely to be explained by thermal pulses and third dredge ups.

Note that the radial increase in the eight stars except for CW Leo are caused by ^{13}CO intensity declining more rapidly than ^{12}CO intensity in the outer envelopes as shown in Fig. 5. It is suggested that this difference in radial behavior between ^{12}CO and ^{13}CO is attributed to selective photodissociation of CO molecules by interstellar UV radiation. M. Saberi et al. (2020) theoretically calculated radial profiles of ^{12}CO/^{13}CO abundance ratio taking into account for selective photodissociation. They found that the ratios in envelopes with $\dot{M} \sim 10^{-5}$ and $\dot{M} \sim 10^{-6}$ $M_\odot$ yr^{-1} start to increase from distances of a thousand to several thousand au from the central star. These results are consistent with the observed radial profiles of the eight stars. On the other hand, in CW Leo, the mass-loss rate derived from the CO emission obtained by our observation is 2.5×10^{-5} $M_\odot$ yr^{-1}, and the radial profile appears to be inconsistent with the results of M. Saberi et al. (2020). However, because our map could not cover the entire envelope as shown in Fig. 1, the integrated line profile in Fig. 2 does not fully reflect the total CO emission, resulting in an underestimation of the mass-loss rate. Additionally the envelope is optically thick ($\tau_{sim} = 2.6$). These factors explain why the radial profile of CW Leo differs from that predicted by M. Saberi et al. (2020).

In the radial profiles of three stars (IW Hya, W Aql, and Y CVn) in Fig. 4, the ^{12}CO/^{13}CO intensity ratios simply decrease in the outer envelopes. M. Saberi et al. (2020) demonstrated that, if interstellar UV radiation is weak, the ^{12}CO/^{13}CO ratio of an envelope with $\dot{M} \sim 10^{-5}$ $M_\odot$ yr^{-1} simply decreases in outer envelope, and this result is consistent with our results. In fact, other observational studies have indicated that photodissociation rate varies with circumstellar environment. For example, in a globular cluster, the photodissociation effect by UV radiation varies with the distance from the center of the cluster (I. McDonald et al. 2015). However, in W Aql, this argument seems to be inconsistent with that of Section 4.1. This can be explained by the shielding effect of circumstellar dust. In the absence of circumstellar dust, UV photons penetrate deeper into the envelope (S. Zhukovska, M. Petrov & T. Henning 2015). Although the interstellar UV radiation is sufficient to photodissociate CO molecules in the outer region of the dust envelope, the CO gas within the dust envelope is not significantly photodissociated because the dust envelope is shielding the gas from interstellar UV radiation. Therefore, in W Aql, the CO gas envelope is smaller than the dust envelope, and also the radial profile of ^{12}CO/^{13}CO intensity ratio is similar to that of the weaker UV-irradiated envelope modelled by M. Saberi et al. (2020).

The radius at which the observed ^{12}CO/^{13}CO ratio begins to change shows a dependence on chemical types. For O-rich and S stars, the increase typically occurs at ∼2000–8000 au, consistent with the predicted onset of selective photodissociation (M. Saberi et al. 2020). Two exceptions among O-rich and S stars are IW Hya and W Aql, whose ratios begin to decline at larger radii of ∼12 000 and 20 000 au, respectively, which are roughly consistent with the predictions of M. Saberi et al. (2020) when the interstellar UV radiation field is weaker. In contrast, C-rich stars show a wider diversity. While the ratios in Y CVn and CQ Pyx begin to change from only a few thousand au, RW LMi, RAFGL 618, and LP And exhibit such changes only beyond ∼8000–10 000 au (CW Leo is excluded here because its radial profile is likely influenced by optical depth effect). If this difference in the transition radius among C-rich stars were primarily driven by the effectiveness of selective photodissociation set by CO density, one would expect a correlation with the mass-loss rate. In fact, Y CVn has a mass-loss rate roughly two orders of magnitude lower than the other C-rich stars and shows a small transition radius (a few 10^3 au). However, CQ Pyx exhibits a similarly small transition radius despite having a mass-loss rate comparable to RW LMi, RAFGL 618, and LP And. Therefore, the difference in transition radius among the C-rich stars cannot be explained by $\dot{M}$ alone; additional factors such as dust shielding and the strength of the interstellar UV field. Furthermore, the observed ^{12}CO/^{13}CO ratios tend to be lower in O-rich and S stars ($\lesssim$5–40) and higher in C-rich stars (up to ∼110). These differences seem to suggest that the effectiveness of selective photodissociation varies with chemical type, driven by envelope density, CO self-shielding, and dust shielding. Variations in interstellar UV radiation

field may also change the degree of selective photodissociation (I. McDonald et al. 2015).

Additionally, the observed ^{12}CO/^{13}CO ratios with chemical types fall roughly within the range of isotopic ratios found in normal AGB stars without shells (∼6–70 for M-type, ∼2–70 for S type, ∼2–100 for carbon stars; S. Ramstedt & H. Olofsson 2014). This consistency implies that the commonly observed ^{12}CO/^{13}CO ratios in normal AGB stars are likely influenced not only by intrinsic changes in the ^{12}C/^{13}C ratio caused by nucleosynthesis, but also by selective photodissociation in their outer envelopes.

Of the stars mapped in NESS–NRO, Y CVn has been found to exhibit a shell-like dust distribution with a radius of ∼ 180 arcsec (H. Izumiura et al. 1996). However, we observed a CO gas envelope with a radius of ∼15 arcsec and could not find the shell structure because the structure is outside the map size of our observations. Even if the map size was large enough to cover the structure, the shell structure would have not been detected in CO emission, because the radius of the dust shell is 12 times larger than that of the CO gas envelope and the CO molecules in the very outer region are expected to be further photodissociated by UV radiation.

4.2 Optical depth effects on detectability of thermal pulse signature

The comparison between the simulated and observed mass-loss rates was performed to evaluate the reliability of the optical depths inferred from our radiative-transfer models. For stars where the simulated mass-loss rates are consistent with the observed mass-loss rates within a factor of ∼2, the corresponding optical depths can be regarded as reasonably reliable, suggesting that the adopted radiative-transfer treatment and assumed density distribution adequately capture the essential structure of the envelopes. In six stars (CW Leo, *o* Cet, WX Psc, RW LMi, χ Cyg, and IK Tau), however, larger discrepancies are seen, and these likely arise from additional effects not included in our simplified models.

For CW Leo, as previously mentioned, the observed maps did not cover the entire envelopes, which likely leads to underestimating the flux. Because the observed mass-loss rates are based on CO line profile integrated over the entire envelope, the mass-loss rate is underestimated due to the underestimating flux.

o Cet and WX Psc are known to have asymmetric structures, and their deviation from spherical symmetry likely accounts for the discrepancies with the spherical model in our simulations. RW LMi shows arc-like features in its envelope in HC_3N line observations (M. J. Claussen et al. 2011; H. Kim et al. 2015), suggesting that inhomogeneities in the density distribution are responsible for the discrepancy in the mass-loss rate.

χ Cyg is an S-type star, for which the assumed CO abundance $f_{\rm CO}$ is likely to be uncertain. In addition, several stars (WX Psc, IK Tau, IW Hya, RAFGL 618, CQ Pyx, RW LMi, W Aql, and χ Cyg) show smaller ^{13}CO envelopes compared to ^{12}CO (the size ratio, $\mathrm{CSE}_{^{12}\mathrm{CO}}/\mathrm{CSE}_{^{13}\mathrm{CO}} \gtrsim 1.5$) as shown in Table 4, where the size ratios are derived from the observed CSE sizes. This suggest that photodissociation affects their outer CSEs, directly impacting on the derived mass-loss rates. This is because the photodissociation reduces CO density in outer CSE, thereby lowering its contribution to the observed line intensity. However, our models do not take into account for the photodissociation effect. As a result, when matching the simulated spectra to the observations, the models generally reduce the overall CO density to compensate for the artificially strong outer contribution, which leads to an underestimation of the true mass-loss rates. Nevertheless, this general picture may not apply uniformly to all stars. Among the stars with large CSE size ratios, IK Tau, and χ Cyg are particularly notable because their modelled optical depths are relatively small. This imply that self-shielding is weak and that selective photodissociation is unlikely significant in these stars. In addition, a comparison of the ^{12}CO/^{13}CO CSE size ratios with the simulated optical depths yields a moderate correlation (correlation coefficient ∼ 0.45), indicating that selective photodissociation alone cannot explain the observed differences in the CSE sizes. These results suggest that the CSE size and CO density structure at the outer envelope are influenced not only by photodissociation but also by other factors, such as variations in the interstellar UV field, dust shielding, or uncertainties in the CO abundance. Consequently, these additional effects is likely to contribute to the discrepancies between the simulated and observed mass-loss rates. However, for WX Psc, it should be noted that the ^{13}CO CSEs are clearly non-spherical. Since the ^{13}CO CSE sizes used in the ratio were estimated from the average of the major and minor axes, the derived ^{12}CO/^{13}CO CSE size ratios are likely not accurately reflect the impact of photodissociation in WX Psc.

If the observed envelopes were optically thick, only the surface layers would be observable, making it difficult to accurately trace mass-loss history. However, the optical depths estimated from our simulations (Table 4) are relatively small for most targets ($\tau_{\rm sim} \lesssim 0.5$), indicating that the envelopes are optically thin even toward the CSE centers. This implies that the outer regions should be even thinner, and thus the optical depth effects are unlikely to obscure thermal-pulse signatures in most stars. In a few objects with $\tau_{\rm sim} \gtrsim 1$, the envelopes may be optically thick enough for such features to be partially suppressed in the radial profiles. These optically thick stars tend to show rounded or parabolic CO line profiles, which is consistent with their larger inferred optical depths. Nevertheless, because of velocity gradient in expanding CSE, CO line kinematics is generally not very sensitive to the overall optical depth. If some velocity components are optically thick, they may locally obscure such features, but the absence of thermal pulses and third dredge up signatures in our data is more likely to be true rather than an opacity effect. In conclusion, there exists no signatures for thermal pulses or third dredge up in the material ejected within the last ∼1500–13 000 yr, and also the ^{12}CO/^{13}CO ratio changes confirmed at ∼1000–40 000 au from central star are caused by selective photodissociation by the interstellar UV radiation. Note that this timescale was calculated from the radius of the envelopes and terminal velocity of the wind.

4.3 The origin of an aspherical envelope morphology

4.3.1 o Cet

o Cet is one of the most intensely observed AGB stars and hosts a binary system (L. D. Matthews, M. J. Reid & K. M. Menten 2015). This star has been observed in far and near-UV bands at wavelengths of 151.6 and 226.7 nm, exhibiting a gas tail extending over ∼ 2.7° and a bow shock in the forward direction (D. C. Martin et al. 2007). In addition, an H I tail of ∼ 12 arcmin was observed with the VLA (L. D. Matthews et al. 2008). These observations also revealed narrow gas streams to the north and south of the central binary.

In our velocity-integrated ^{13}CO($J = 1 \rightarrow 0$) map (Fig. 1), the envelope is elongated towards the southwest, consistent with the root of the southern gas stream seen in the UV and HI data. ALMA observations in CO and SiO emission have confirmed a southwestern outflow on smaller spatial scales (D. T. Hoai et al. 2020; P. T. Nhung et al. 2022). Those studies identified a blueshifted outflow around

∼47–49 km s^{-1}. We also detect a blueshifted component at ∼47 km s^{-1} in the same direction, on a spatial scale larger by a factor of ∼10.

The ^{13}CO map in Fig. 1 shows noticeably weaker emission on the northwestern side compared to the ^{12}CO map. A likely explanation is that the mass-loss is characterized by bipolar outflows, producing dense material along the specific directions, but the ejected gas has gradually dispersed, forming an approximately spherical distribution traced by ^{12}CO emission. In the lower-density directions, ^{13}CO molecules are more easily photodissociated because their self-shielding is weaker than that of ^{12}CO molecules. As a result, the remaining ^{13}CO emission becomes concentrated along the denser bipolar regions, and the ^{13}CO emission is much fainter than ^{12}CO emission on the northwestern side. In addition, anisotropic illumination by the interstellar radiation field toward the northwest may further enhance this effect, reducing the ^{13}CO emission relative to ^{12}CO.

Furthermore, D. T. Hoai et al. (2020) and P. T. Nhung et al. (2022) detected redshifted CO and SiO emission in the south–west region. The redshifted and blueshifted components observed in the same region interpreted as signatures of shock-wave propagation: the redshifted component is generated from the gas ejected earlier in the direction, and followed by the propagation of the shock wave in the direction, resulting in the emission of the blueshifted component. However, our observations detected only blueshifted component at the center of the envelope. This suggests that the shock wave does not propagate to the distances of ∼2000 au from the binary observed by NESS–NRO.

4.3.2 *WX Psc*

WX Psc has a bipolar structure that has been confirmed by several observations (e.g. A. Castro-Carrizo et al. 2010). K. H. Hofmann et al. (2001) confirmed a bipolar structure toward the north direction by near-infrared observation, and D. Vinković et al. (2004) suggests that bipolar jet had swept up circumstellar material. Futhermore, CO emission observations by A. Castro-Carrizo et al. (2010) revealed an elongated gas distribution in the northwest–southeast direction.

Our ^{13}CO observations also reveal an elongation along the same direction. In particular, the ^{13}CO distribution appears weaker toward the east, west, and south sides. While ^{12}CO is typically the best tracer of a bipolar outflows, such elongation is not evident in our ^{12}CO map. This suggests that the aspherical morphology seen in ^{13}CO emission cannot be attributed solely to bipolar outflow. As discussed for *o* Cet, a likely explanation is that mass-loss has bipolar outflows, producing denser gas along polar directions, while lower density regions are more vulnerable to selective photodissociation of ^{13}CO due to weaker self-shielding. In addition, anisotropic illumination by the interstellar radiation field toward the north–west may further enhance this effect, reducing the ^{13}CO emission relative to ^{12}CO.

4.3.3 *RAFGL 618*

RAFGL 618 (=CRL 618) has two opposite lobes created by twin collimated jets observed with the *Hubble Space Telescope* (B. Balick et al. 2013). The lobes have a length of ∼ 7 arcsec and extend from the central binary in east-west direction. The length of the lobes and a velocity of the jets suggest that the age of the lobes is ∼100 yr (C.-F. Lee & R. Sahai 2003; B. Balick et al. 2013).

In our data, ^{12}CO emission appears nearly spherical (Fig. B2), whereas ^{13}CO emission shows an elongated morphology, as shown in Fig. B3. In channel maps of the ^{13}CO emission, the elongated structure at −26.5 and −12.5 km s^{-1} is aligned with the jet axis. C. Lee et al. (2013) and L. Sabin et al. (2014) observed this star with the SMA in CO ($J = 3 \rightarrow 2$) emission at angular resolutions of ∼ 0.3 arcsec and ∼ 2.2 arcsec, respectively, and also confirmed elongation in the same direction. A likely interpretation, similar to the case of *o* Cet and WX Psc, is that ^{13}CO molecules are selectively photodissociated in the lower density regions due to weaker self-shielding, leaving emission concentrated along denser outflow directions. Anisotropic interstellar UV radiation fields may further enhance this asymmetry.

4.3.4 *SV Peg*

The envelope in ^{12}CO emission is elongated toward the south, as shown in Fig. 1. This elongation appears to be a bipolar outflow or a tail similar to that of *o* Cet. However, in channel maps in Fig. B1, the elongated envelope is confirmed only at the velocities of 1.0 and 2.2 km s^{-1}. Additionally, the averaged proper motion of this star is estimated to be 11.59 ± 0.54 and –8.63 ± 0.44 mas yr^{-1} in Right Ascension and Declination directions (H. Sudou et al. 2019), respectively. Thus, there is no correlation between the direction of the elongation and the proper motion. Therefore, the elongated envelope is not caused by a bipolar outflow or a fast proper motion. An alternative interpretation is that the unusual channel maps may be contaminated by foreground (or background) interstellar clouds or the overlap of two AGB stars. A SIMBAD search, which uses data from the Gaia DR3 catalogue (Gaia Collaboration 2022), reveals the nearest star, TYC 2728−580−1, located ∼ 108 arcsec from SV Peg at a position angle of ∼ 262° (west–southwest). In contrast, the observed CSE is elongated toward the south at a position angle of ∼ 184° and is only seen at $v_{\rm LSR} = 1.0$–2.2 km s^{-1}. Although the radial velocity of TYC 2728−580−1 is close to these channels ($v_{\rm LSR} \sim 1.7$ km s^{-1}), the positional directions are inconsistent. If the elongation originated from this star, the elongation would appear toward the west rather than the south. Furthermore, TYC 2728-580-1 is not classified as an AGB star in SIMBAD. Therefore, an overlap with another CSE is ruled out, and interstellar CO remains more plausible explanation.

5 CONCLUSION

In order to reveal extended and cold gas envelopes, we have conducted mapping observations of 42 AGB stars in ^{12}CO and ^{13}CO ($J = 1 \rightarrow 0$) emission using the Nobeyama 45 m radio telescope. Out of 42 stars, 23 and 14 stars were detected in ^{12}CO and ^{13}CO emission, respectively. Comparing the envelope sizes in ^{12}CO ($J = 1 \rightarrow 0$) obtained by NESS–NRO and ($J = 3 \rightarrow 2$) obtained by NESS–JCMT in the four stars (CW Leo, IK Tau, W Aql, and TX Cam), the envelopes sizes in ^{12}CO ($J = 1 \rightarrow 0$) were twice or more extended than those in ^{12}CO ($J = 3 \rightarrow 2$) emission. This result suggest that the NESS–NRO observations in ^{12}CO ($J = 1 \rightarrow 0$) emission revealed a colder extended gas envelopes than those traced by ^{12}CO ($J = 3 \rightarrow 2$) emission to trace older mass-loss history.

The comparison between the gas envelopes traced by ^{12}CO ($J = 1 \rightarrow 0$) emission and the dust envelopes traced by 870 μm continuum indicates the photodissociation states of outer envelopes. Large CO ($J = 1 \rightarrow 0$) gas envelopes (>10 000 au) tend to have a smaller size than the dust envelopes, whereas relatively smaller CO gas envelopes ($\lesssim$ 10 000 au) tend to have a similar size to dust envelopes. We interpret this tendency as the outcome of photodissociation of CO molecules depending on the gas density along the envelope

expansion. In low-density outer regions, CO molecules are more easily photodissociated by interstellar UV radiation, leading to a smaller CO ($J = 1 \rightarrow 0$) envelope compared to the dust envelope. An exception was CW Leo, whose envelope is optically thick and therefore less affected by photodissociation. Thus, its ^{12}CO ($J = 1 \rightarrow 0$) envelope is larger than the dust envelope.

In order to trace detached gas shells as a signature of thermal pulses and third dredge ups, we investigated radial variation of ^{12}CO/^{13}CO ratio from the center to outer envelope. We found that the ^{12}CO/^{13}CO intensity ratio increases along the radial direction for nine AGB stars (IK Tau. WX Psc, V1300 Aql, CW Leo, RW LMi, RAFGL 618, LP And, CQ Pyx, and χ Cyg). However, the increase of ^{12}CO/^{13}CO ratio is caused by a steep radial decrease of ^{13}CO intensity rather than a radial increase of ^{12}CO intensity. This implies that a underlying cause of this behavior is selective photodissociation of CO molecules by interstellar UV radiation, not thermal pulses or third dredge ups. In addition, ^{12}CO/^{13}CO intensity ratio decreases monotonically towards the outer envelope of three stars (IW Hya, W Aql, Y CVn), suggesting that UV radiation fields are relatively weak in their surrounding environments.

Furthermore, we estimated the optical depths of the observed envelopes using radiative transfer simulations and found that the ^{12}CO emission is generally optically thin, with $\tau \lesssim 0.5$ for most targets. Therefore, the absence of detached shell signatures in our data is not attributed to optical depth effect.

In conclusion, we found no signature of thermal pulses or third dredge ups in the material ejected within the last 1500–13 000 yr, and also most of the ^{12}CO/^{13}CO changes at ∼1000–40 000 au from the central star are attributed to selective photodissociation by interstellar UV radiation.

Additionally, the envelopes of four stars (*o* Cet, WX Psc, SV Peg, and RAFGL 618) exhibit aspherical morphologies. In *o* Cet, WX Psc, and RAFGL 618, the aspherical envelopes can be explained by bipolar outflows and selective photodissociation. On the other hand, the aspherical envelope of SV Peg may be contaminated by foreground (or background) interstellar clouds.

ACKNOWLEDGEMENTS

We are grateful to the Nobeyama Radio Observatory staff members for their assistance and observation support. The Nobeyama 45-m radio telescope is operated by Nobeyama Radio Observatory, a branch of the National Astronomical Observatory of Japan. We also appreciate the supports by the students in Kagoshima University for the observations, and Yoshito Shimajiri for his advice on data analysis. The publication of this paper was supported by Amanogawa Galaxy Astronomy Research Center (AGARC), Kagoshima University. KA was supported by Japan Society for the Promotion of Science (JSPS) Fellowship for Young Researchers (Program ID: 23KJ1777). HI is supported by JSPS KAKENHI grant number JP 16H02167. JH thanks the support of NSFC project 11873086. SHJW acknowledges support from the Research Foundation Flanders (FWO) through grant 1285221N. This work is sponsored (in part) by the Chinese Academy of Sciences (CAS), through a grant to the CAS South America Center for Astronomy (CASSACA). This work was also partly supported by the Spanish programme Unidad de Excelencia María de Maeztu CEX2020-001058-M, financed by MCIN/AEI/10.13039/501100011033. JPM acknowledges research support by the National Science and Technology Council of Taiwan under grant NSTC 112-2112-M-001-032-MY3. HK acknowledges the support by the National Research Foundation of Korea (NRF) grant (no. RS-2021-NR058398) and the Korea Astronomy and Space Science Institute (KASI) grant (Project no. 2025184102), both funded by the Korean government (MSIT). SS acknowledges funding from the UNAM–PAPIIT programme IA104824. IM and AAZ acknowledge support from the UK Science and Technology Facilities Council under grant ST/P000649/1. FK acknowledges support from the Spanish Ministry of Science, Innovation and Universities, under grant number PID2023-149918NB-I00. This work was also partly supported by the Spanish programme Unidad de Excelencia María de Maeztu CEX2020-001058-M, financed by MCIN/AEI/10.13039/501100011033.

DATA AVAILABILITY

The CO ($J = 1 \rightarrow 0$) emission data obtained with NRO 45 m telescope are accessed from the Nobeyama-45m/ASTE Science Data Archive at https://nobeyama-archive.nao.ac.jp/user/index.html. The CO ($J = 3 \rightarrow 2$) emission and 870 μm continuum data obtained with JCMT were provided by T. E. Dharmawardena et al. (2018) and P. Scicluna et al. (2022). The derived data generated in this research will be shared on reasonable request to the corresponding author. Catalogues containing all data in this study are available at https://evolvedstars.space.

REFERENCES

Andriantsaralaza M., Ramstedt S., Vlemmings W. H. T., De Beck E., 2022, A&A, 667, 28
Bailer-Jones C. A. L., Rybizki J., Fouesneau M., Demleitner M., Andrae R., 2021, AJ, 161, 147
Balick B., Huarte-Espinosa M., Frank A., Gomez T., Alcolea J., Corradi R. L. M., Vinković D., 2013, ApJ, 772, 11
Bergeat J., Knapik A., Rutily B., 2001, A&A, 369, 178
Castro-Carrizo A. et al., 2010, A&A, 523, A59
Claussen M. J., Sjouwerman L. O., Rupen M. P., Olofsson H., Schöier F. L., Bergman P., Knapp G. R., 2011, ApJ, 739, L5
Decin L. et al., 2020, Science, 369, 1497
Dharmawardena T. E. et al., 2018, MNRAS, 479, 536
Emerson D. T., Graeve R., 1988, A&A, 190, 353
Gaia Collaboration, 2023, A&A, 674, A1
Gottlieb C. A. et al., 2022, A&A, 660, 57
Groenewegen M. A. T., Baas F., Blommaert J. A. D. L., Stehle R., Josselin E., Tilanus R. P. J., 1999, A&AS, 140, 197
Habing H. J., Olofsson H., 2004, Asymptotic Giant Branch Stars. Springer, Berlin
Habing H. J., Olofsson Hans, Habing H. J., Olofsson H., eds, 2003, in Asymptotic Giant Branch Stars. Springer, New York, Berlin
Heras A. M., Hony S., 2005, A&A, 439, 171
Herwig F., 2005, ARA&A, 43, 435
Hoai D. T., Tuan-Anh P., Nhung P. T., Darriulat P., Diep P. N., Phuong N. T., Thai T. T., 2020, MNRAS, 495, 943
Hofmann K. H., Balega Y., Blöcker T., Weigelt G., 2001, A&A, 379, 529
Holland W. S. et al., 2013, MNRAS, 430, 2513
Imai H., He J.-H., Nakashima J.-I., Ukita N., Deguchi S., Koning N., 2009, PASJ, 61, 1365
Izumiura H., Hashimoto O., Kawara K., Yamamura I., Waters L. B. F. M., 1996, A&A, 315, L221
Kamazaki T. et al., 2012, PASJ, 64, 29
Karakas A. I., Lattanzio J. C., 2014, PASA, 31, 62
Kastner J. H., Wilson E., 2021, ApJ, 922, 9
Kim H. et al., 2015, ApJ, 814, 61
Knapp G. R., Morris M., 1985, ApJ, 303, 640
Lee C.-F., Sahai R., 2003, ApJ, 586, 319
Lee C., Sahai R., Sánchez Contreras C., Huang P., Hao Tay J. J., 2013, ApJ, 777, 9
Maercker M. et al., 2012, Nature, 490, 232
Maercker M. et al., 2024, A&A, 687, A112
Mamon G. A., Glassgold A. E., Huggins P. J., 1988, ApJ, 328, 797

Martin D. C. et al., 2007, Nature, 448, 780
Matthews L. D., Libert Y., Gérard E., Le Bertre T., Reid M. J., 2008, ApJ, 684, 603
Matthews L. D., Reid M. J., Menten K. M., 2015, ApJ, 808, 10
Mattsson L., Höfner S., Herwig F., 2007, A&A, 470, 339
McDonald I. et al., 2015, MNRAS, 453, 4324
McDonald I., Zijlstra A. A., Boyer M. L., 2012, MNRAS, 427, 343
McDonald I., Zijlstra A. A., Watson R. A., 2017, MNRAS, 471, 770
Michalik D., Lindegren L., Hobbs D., 2015, A&A, 574
Minamidani T. et al., 2016, in Holland W. S., Zmuidzinas J., eds, SPIE Conf. Ser. Vol. 9914, Millimeter, Submillimeter, and Far-Infrared Detectors and Instrumentation for Astronomy VIII. SPIE, Bellingham, p. 99141Z
Nhung P. T., Hoai D. T., Tuan-Anh P., Darriulat P., Diep P. N., Ngoc N. B., Thai T. T., 2022, ApJ, 927, 16
Olofsson H., Bergman P., Lucas R., Eriksson K., Gustafsson B., Bieging J. H., 2000, A&A, 353, 583
Olofsson H., Carlstrom U., Eriksson K., Gustafsson B., Willson L. A., 1990, A&A, 230, L13
Olofsson H., Eriksson K., Gustafsson B., Carlstrom U., 1993, ApJS, 87, 267
Pols O. R., Tout C. A., Lattanzio J. C., Karakas A. I., 2001, in Podsiadlowski P., Rappaport S., King A. R., D'Antona F., Burderi L., eds, ASP Conf. Ser. Vol. 229, Evolution of Binary and Multiple Star Systems. Astron. Soc. Pac., San Francisco, p. 31
Ramstedt S. et al., 2020, A&A, 640, 28
Ramstedt S., Olofsson H., 2014, A&A, 566, A145
Ramstedt S., Schöier F. L., Olofsson H., Lundgren A. A., 2008, A&A, 487, 645
Saberi M., Olofsson H., Vlemmings W. H. T., De Beck E., Khouri T., Ramstedt S., 2020, A&A, 638, A99
Saberi M., Vlemmings W. H. T., De Beck E., 2019, A&A, 625, 13
Sabin L., Zhang Q., Zijlstra A. A., Patel N. A., Vázquez R., Zauderer B. A., Contreras M. E., Guillén P. F., 2014, MNRAS, 438, 1794
Schöier F. L., Lindqvist M., Olofsson H., 2005, A&A, 436, 633
Schröder K. P., Winters J. M., Sedlmayr E., 1999, A&A, 349, 898
Scicluna P. et al., 2022, MNRAS, 512, 1091
Steffen M., Schönberner D., 2000, A&A, 357, 180
Steffen M., Szczerba R., Schoenberner D., 1998, A&A, 337, 149
Sudou H. et al., 2019, PASJ, 71, 16
van der Tak F. F. S., Black J. H., Schöier F. L., Jansen D. J., van Dishoeck E. F., 2007, A&A, 468, 627
van Leeuwen F., 2007, A&A, 474, 653
Vinković D., Blöcker T., Hofmann K. H., Elitzur M., Weigelt G., 2004, MNRAS, 352, 852
Vlemmings W. H. T. et al., 2013, A&A, 556, 6
Wagenhuber J., Groenewegen M. A. T., 1998, A&A, 340, 183
Wilson T. L., Rohlfs K., Hüttemeister S., 2013, Tools of Radio Astronomy. Springer, Berlin Heidelberg
Zhukovska S., Petrov M., Henning T., 2015, ApJ, 810, 14

APPENDIX A: LIST OF TARGET STARS IN SINGLE-POINT OBSERVATIONS

Table A1 shows a list of target sources, antenna temperature, and RMS noise level in our single-point observations. We carried out the single-point observations towards 208 sources, which included 42, 71, 58, and 37 in extreme, high, intermediate, and low sources in NESS subsample. Detailed definition and classification of the NESS subsample are described in (P. Scicluna et al. 2022). 96 and 34 stars were detected in ^{12}CO and ^{13}CO emission brighter than 3σ. Detailed results and statistical discussion with the full data set of the single-point observations will be presented in a future paper.

Table A1. List of targets sources in the staring observations.

IRAS PSC ID	Target	NESS subsample	$T_{A}{}^{12}$CO (K)	$\sigma_{^{12}\mathrm{CO}}$ (K)	$T_{A}{}^{13}$CO (K)	$\sigma_{^{13}\mathrm{CO}}$ (K)
(1)	(2)	(3)	(4)	(5)	(6)	(7)
03149+3244	BD+32 599	extreme	–	0.067	–	0.035
03206+6521	OH 138.0 +7.2	extreme	–	0.052	–	0.030
04395+3601	RAFGL 618	extreme	4.448	0.056	0.391	0.029
05073+5248	NV Aur	extreme	0.846	0.047	0.225	0.027
05251–1244	IC 418	extreme	0.221	0.044	–	0.019
05377+3548	IRAS 05377+3548	extreme	–	0.050	1.670	0.025
05388–0147	IRAS 05388–0147	extreme	–	0.085	1.120	0.038
06050–0623	IRAS 06050–0623	extreme		0.148	1.530	0.064
06193–0349	V654 Mon	extreme	0.343	0.050	0.110	0.023
17239–2812	IRAS 17239–2812	extreme	–	0.078	–	0.027
17441–2411	RAFGL 5385 (= Silkworm nebula)	extreme	0.149	0.034	0.130	0.034
18155–1206	IRAS 18155–1206	extreme	2.220	0.079	0.448	0.034
18162–0246	RAFGL 5466	extreme	–	0.061	0.110	0.027
18216–1617	RAFGL 2143	extreme	0.203	0.068	–	0.024
18303–0519	IRAS 18303–0519	extreme	–	0.072	–	0.028
18437–0643	V440 Sct	extreme	–	0.072	–	0.031
18535+0726	OH 40.1 +2.4	extreme	–	0.064	–	0.030
18595+0107	IRAS 18595+0107	extreme	–	0.090	1.750	0.030
19161+2343	RAFGL 2362	extreme	0.281	0.043	–	0.021
19244+1115	IRC +10420	extreme	0.245	0.039	–	0.019
19288+2923	IRAS 19288+2923	extreme	–	0.054	–	0.027
19327+3024	HD 184738	extreme	–	0.035	–	0.019
19396+1637	HM Sge (= NOVA Sge 1975)	extreme	–	0.050	–	0.027
19422+3506	RAFGL 2445	extreme	0.134	0.040	–	0.019
19566+3423	IRAS 19566+3423	extreme	...	0.059	–	0.026

Table A1 – *continued*

IRAS PSC ID	Target	NESS subsample	$T_{A}{}^{12}\mathrm{CO}$ (K)	$\sigma_{^{12}\mathrm{CO}}$ (K)	$T_{A}{}^{13}\mathrm{CO}$ (K)	$\sigma_{^{13}\mathrm{CO}}$ (K)
(1)	(2)	(3)	(4)	(5)	(6)	(7)
19597+3327A	2MASX J20013735+3335282	extreme	15.867	0.057	4.171	0.026
20002+3322	IRAS 20002+3322	extreme	3.203	0.069	1.326	0.034
20028+3910	IRAS 20028+3910	extreme	...	0.073	–	0.034
20081+2720	IRAS 20081+2720	extreme	3.847	0.052	2.467	0.026
20547+0247	U Equ	extreme	...	0.057	–	0.026
21305+2118	IRAS 21305+2118	extreme	...	0.054	–	0.026
22133+5837	V653 Cep	extreme	...	0.028	–	0.028
22177+5936	NSV 25875	extreme	2.603	0.065	1.102	0.031
22540+6146	2MASX J22560350+6202554	extreme	–	0.062	1.520	0.031
22544+6141	IRAS 22544+6141	extreme		0.078	–	0.046
22548+6147	IRAS 22548+6147	extreme	0.600	0.093	1.0404	0.057
23541+7031	PN M 2–56	extreme	0.237	0.060	–	0.030
19178–2620	OH 012.11–17.19 (= [LFO93] 1917–26)	extreme	0.176	0.024	0.033	0.008
18298–2111	RAFGL 5501	extreme	–	0.027	–	0.010
18502–0253	NSV 11461	extreme	0.352	0.019	–	0.009
18139–1952	IRAS 18139–1952	extreme	2.332	0.024	3.56979	0.010
17565–2035	IRAS 17565–2035	extreme	0.438	0.024	0.046	0.010
00042+4248	KU And	high	0.374	0.039	0.064	0.017
00213+3817	R And	high	1.167	0.054	0.101	0.025
01037+1219	WX Psc (= IRC +10011)	high	1.511	0.053	0.417	0.025
01159+7220	S Cas	high	0.776	0.056	–	0.028
02185+5622	SU Per	high	–	0.035	–	0.018
02192+5821	S Per	high	–	0.063	–	0.028
02316+6455	V656 Cas	high	0.991	0.060	0.139	0.029
02351–2711	UU For	high	0.349	0.085	–	0.030
02469+5646	W Per	high	–	0.067	–	0.033
03030+5532	IO Per	high	–	0.049	–	0.025
03170+3150	UZ Per	high	–	0.041	–	0.020
03229+4721	V384 Per	high	1.222	0.058	0.190	0.031
04166+4056	IR Per	high	0.223	0.048	0.263	0.024
06250+6134	V Lyn	high	–	0.056	–	0.029
06300+6058	AP Lyn	high	0.577	0.081	–	0.034
06363+5954	U Lyn	high	–	0.036	–	0.089
06500+0829	GX Mon	high	1.495	0.062	0.236	0.033
07585–1242	U Pup	high	–	0.056	–	0.025
15223–0203	OV Ser	high	–	0.063	–	0.028
15255+1944	WX Ser	high	–	0.058	–	0.027
17049–2440	V2548 Oph	high	1.144	0.098	0.184	0.037
17119+0859	V2108 Oph	high	–	0.061	–	0.027
17265–0725	BD-07 4447	high	–	0.063	–	0.028
17297+1747	V833 Her	high	0.898	0.037	0.145	0.018
17361+5746	TY Dra	high	0.139	0.042	–	0.019
17539+1037	IRC +10340	high	–	0.037	–	0.020
18044–2927	HD 165531	high	–	0.103	–	0.036
18076–1034	IRC -10401	high	–	0.028	–	0.028
18194–2708	V5104 Sgr	high	0.537	0.092	–	0.031
18240+2326	V1076 Her	high	1.040	0.060	0.125	0.026
18288–0207	RAFGL 2177	high	–	0.063	0.250	0.026
18349+1023	V1111 Oph	high	0.401	0.064	0.1001	0.033
18397+1738	V821 Her	high	0.372	0.060	0.087	0.032
18501–2132	V2059 Sgr	high	–	0.055	–	0.022
19175–0807	V1420 Aql	high	–	0.090	–	0.037
19296+4331	UV Cyg	high	0.170	0.039	–	0.020
19474–0744	GY Aql	high	–	0.081	–	0.036
19536+3237	V468 Cyg	high	0.331	0.049	–	0.025
20077–0625	V1300 Aql	high	1.526	0.065	0.295	0.029
20440–0105	FP Aqr	high	0.484	0.069	–	0.032
20502+4709	RZ Cyg	high	2.343	0.054	0.561	0.026
21543–1421	HD 208519	high	0.223	0.067	–	0.028
23013+3735	CF And	high	–	0.040	–	0.018
23320+4316	LP And	high	2.637	0.046	0.398	0.025
23365+5159	SV Cas	high	–	0.035	–	0.017

Table A1 – *continued*

IRAS PSC ID	Target	NESS subsample	$T_{A}{}^{12}$CO (K)	$\sigma_{^{12}\mathrm{CO}}$ (K)	$T_{A}{}^{13}$CO (K)	$\sigma_{^{13}\mathrm{CO}}$ (K)
(1)	(2)	(3)	(4)	(5)	(6)	(7)
23420+5618	Z Cas	high	–	0.046	–	0.027
04566+5606	TX Cam	high	0.918	0.017	0.057	0.010
05151+6312	BW Cam	high	0.290	0.019	0.053	0.010
05351–0147	X Ori	high	–	0.022	–	0.011
05411+6957	BX Cam	high	0.261	0.023	0.056	0.014
05559+7430	V Cam	high	0.139	0.016	0.038	0.008
07585–1242	U Pup	high	0.105	0.031	–	0.017
08200–2528	OT Pup	high	–	0.044	–	0.021
08220–0821	FK Hya	high	–	0.024	–	0.014
09116–2439	CQ Pyx	high	1.280	0.024	0.068	0.010
09429–2148	IW Hya	high	0.536	0.021	0.072	0.009
09425+3444	R LMi	high	0.185	0.017	–	0.010
10411+6902	R UMa	high	0.281	0.021	0.040	0.009
11445+4344	AZ UMa	high	0.077	0.018	–	0.011
13172+4547	V CVn	high	–	0.019	–	0.010
14247+0454	RS Vir	high	0.192	0.024	–	0.014
19059–2219	V3880 Sgr	high	0.300	0.031	0.061	0.011
08200–2528	OT Pup	high	0.110	0.022	–	0.007
07209–2540	VY CMa	high	0.280	0.019	–	0.008
06491–0654	HD 50138	high	–	0.017	–	0.008
06349–0121	SY Mon	high	0.102	0.015	–	0.007
06027–1628	17 Lep	high	–	0.022	–	0.009
06176–1036	HD 44179 (= Red Rectangle)	high	0.190	0.018	0.070	0.008
19550–0201	RR Aql	high	0.328	0.014	0.044	0.007
23166+1655	RAFGL 3068	high	0.425	0.007	0.045	0.004
00192–2020	T Cet	intermediate	0.218	0.041	–	0.016
00205+5530	T Cas	intermediate	0.292	0.038	–	0.022
01556+4511	V370 And	intermediate	1.160	0.047	0.148	0.024
04020–1551	V Eri	intermediate	0.181	0.040	–	0.017
05027–2158	T Lep	intermediate	–	0.049	–	0.021
05132+5331	R Aur	intermediate	0.621	0.068	–	0.030
05265–0443	S Ori	intermediate	0.211	0.059	–	0.026
05292+1833	119 Tau	intermediate	–	0.041	–	0.019
05524+0723	alf Ori	intermediate	0.269	0.029	0.080	0.014
15341+1515	tau04 Ser	intermediate	–	0.039	–	0.019
15492+4837	ST Her	intermediate	0.321	0.057	–	0.026
15566+3609	RS CrB	intermediate	–	0.073	–	0.029
16011+4722	X Her	intermediate	–	0.048	–	0.024
16081+2511	RU Her	intermediate	0.185	0.053	–	0.025
16235+1900	U Her	intermediate	–	0.061	–	0.029
17123+1426	alf Her	intermediate	–	0.053	–	0.024
17553+4521	OP Her	intermediate	–	0.047	–	0.023
18359+0847	X Oph	intermediate	0.203	0.051	–	0.024
19232+5008	CH Cyg	intermediate	–	0.078	–	0.035
19503+2219	NS Vul	intermediate	–	0.050	–	0.026
20396+4757	V Cyg	intermediate	2.147	0.132	0.179	0.033
20431+1754	U Del	intermediate	0.289	0.037	–	0.017
21088+6817	T Cep	intermediate	0.435	0.054	–	0.028
21341+4508	W Cyg	intermediate	0.270	0.053	–	0.025
21419+5832	mu. Cep	intermediate	–	0.050	–	0.024
21439–0226	EP Aqr	intermediate	0.350	0.073	0.100	0.030
22017+2806	TW Peg	intermediate	0.222	0.055	–	0.025
22035+3506	SV Peg	intermediate	0.372	0.054	–	0.025
22216+3100	PV Peg	intermediate	–	0.053	–	0.025
22525–2952	V PsA	intermediate	–	0.074	–	0.027
23173+2600	W Peg	intermediate	0.192	0.044	–	0.021
23412–1533	R Aqr	intermediate	–	0.053	–	0.020
08003+3629	SV Lyn	intermediate	0.120	0.011	0.033	0.006
08138+1152	R Cnc	intermediate	–	0.016	–	0.009
09448+1139	R Leo	intermediate	0.234	0.010	0.018	0.005
10491–2059	V Hya	intermediate	2.199	0.023	0.060	0.009
10580–1803	R Crt	intermediate	0.605	0.021	0.033	0.009

Table A1 – *continued*

IRAS PSC ID	Target	NESS subsample	$T_{A^{12}CO}$ (K)	$\sigma_{^{12}CO}$ (K)	$T_{A^{13}CO}$ (K)	$\sigma_{^{13}CO}$ (K)
(1)	(2)	(3)	(4)	(5)	(6)	(7)
12277+0441	BK Vir	intermediate	0.223	0.016	–	0.008
12380+5607	Y UMa	intermediate	0.474	0.015	–	0.009
12427+4542	Y CVn	intermediate	0.526	0.021	0.244	0.012
13001+0527	RT Vir	intermediate	0.252	0.018	–	0.009
13269–2301	R Hya	intermediate	0.217	0.024	–	0.011
13462–2807	W Hya	intermediate	0.196	0.028	–	0.012
14371+3245	RV Boo	intermediate	0.167	0.013	–	0.007
14390+3147	RW Boo	intermediate	–	0.051	–	0.033
20038–2722	V1943 Sgr	intermediate	0.173	0.021	–	0.008
21044–1637	RS Cap	intermediate	0.086	0.020	–	0.010
20248–2825	T Mic	intermediate	0.215	0.036	–	0.014
19007–2247	SU Sgr	intermediate	0.190	0.029	–	0.012
06036–2411	S Lep	intermediate	–	0.021	–	0.008
05592–0221	V352 Ori	intermediate	–	0.015	–	0.007
15214–2244	RS Lib	intermediate	–	0.038	–	0.013
08375–1707	AK Hya	intermediate	0.234	0.022	–	0.008
23558+5106	R Cas	intermediate	0.916	0.055	0.1048	0.0281
16418+5459	S Dra	intermediate	0.058	0.011	–	0.033
09076+3110	RS Cnc	intermediate	0.499	0.034	–	0.015
05028+0106	W Ori	intermediate	0.094	0.014	–	0.007
09251–0826	alf Hya (= S SVS 75)	low	–	0.018	–	0.008
11284+6936	lam Dra (= S ZI 888)	low	–	0.024	–	0.014
11358+0824	ome Vir	low	–	0.021	–	0.012
13039+2253	FS Com	low	–	0.011	–	0.006
13388+5456	IQ UMa	low	–	0.022	–	0.012
14059+4405	BY Boo	low	–	0.020	–	0.011
14059+4405	RX Lep	low	–	0.010	–	0.005
23154+4844	8 And (= S ZI 2130)	low	–	0.012	–	0.006
21402+4532	V1339 Cyg	low	–	0.011	–	0.006
22366+5632	V416 Lac	low	–	0.007	–	0.003
18578+2244	V387 Vul	low	–	0.014	–	0.007
21397+0527	NSV 13848	low	–	0.012	–	0.005
22023+6252	MO Cep	low	–	0.013	–	0.006
23142–0759	chi Aqr	low	–	0.017	–	0.008
23077+3329	V345 Peg	low	–	0.011	–	0.006
20451–0512	EN Aqr	low	–	0.024	–	0.011
20372–1818	NSV 25208	low	–	0.019	–	0.008
15097+1909	FL Ser	low	–	0.011	–	0.052
15011–2505	sig Lib	low	–	0.022	–	0.008
10350–1307	U Hya (= HD 92055)	low	0.789	0.015	0.032	0.006
08461–2827	AK Pyx	low	–	0.019	–	0.006
07207+8230	VZ Cam	low	–	0.010	–	0.004
07190–2547	MZ CMa	low	–	0.019	–	0.008
07104+1614	BQ Gem	low	0.074	0.011	–	0.005
06199+2232	mu. Gem	low	–	0.009	–	0.004
06124–0615	gam Mon	low	0.476	0.026	0.142	0.013
05271–0107	CI Ori	low	–	0.014	–	0.006
03557–1339	gam Eri	low	–	0.013	–	0.006
03377+6303	BD Cam	low	0.105	0.021	–	0.005
03173+2852	HD 20644	low	0.096	0.011	0.027	0.005
03172–2156	tau04 Eri	low	–	0.016	–	0.006
02596+0353	alf Cet	low	–	0.013	–	0.006
02327+3428	15 Tri (= S ZI 136)	low	–	0.011	–	0.005
01579–0845	AR Cet	low	–	0.012	–	0.006
01069+3521	bet And (= NSV 414)	low	–	0.011	–	0.005
00121–1912	AE Cet	low	–	0.021	–	0.009
21417+0938	eps Peg	low	–	0.014	–	0.006

Note. The different columns list (1) IRAS PSC ID, (2) the target name, (3) NESS subsample referenced by P. Scicluna et al. (2022), (4) anntena temperature in CO emission, (5) RMS noise level for CO spectra at 115 GHz, (6) anntena temperature in ^{13}CO emission and (7) RMS noise level for ^{13}CO spectra at 110 GHz. Non detections are represented by dots.

APPENDIX B: CHANNEL MAPS OF THE ASPHERICAL ENVELOPES

This appendix presents aspherical envelopes. Fig. B1 shows channel maps of SV Peg in ^{12}CO emission. Figs B2 and B3 show channel maps of RAFGL 618 in ^{12}CO and ^{13}CO emission, respectively.

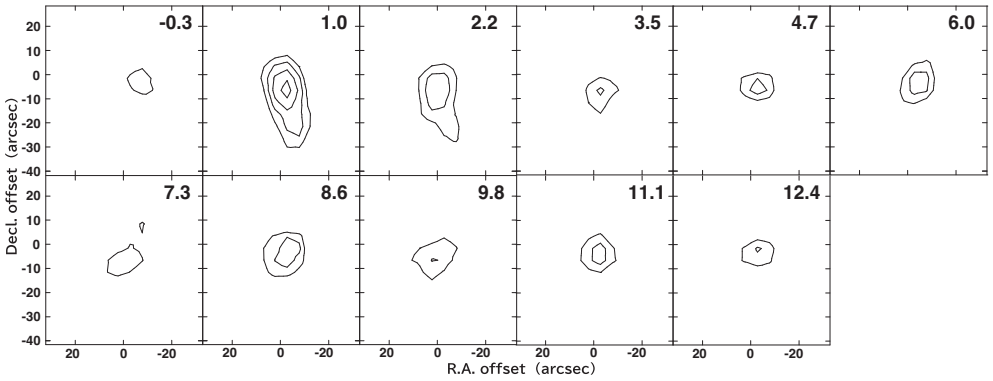

Figure B1. ^{12}CO ($J = 1 \rightarrow 0$) emission channel maps of SV Peg. The contour levels are $1\sigma \times$ (3,4,5,6), where 1 σ = 0.05 K.

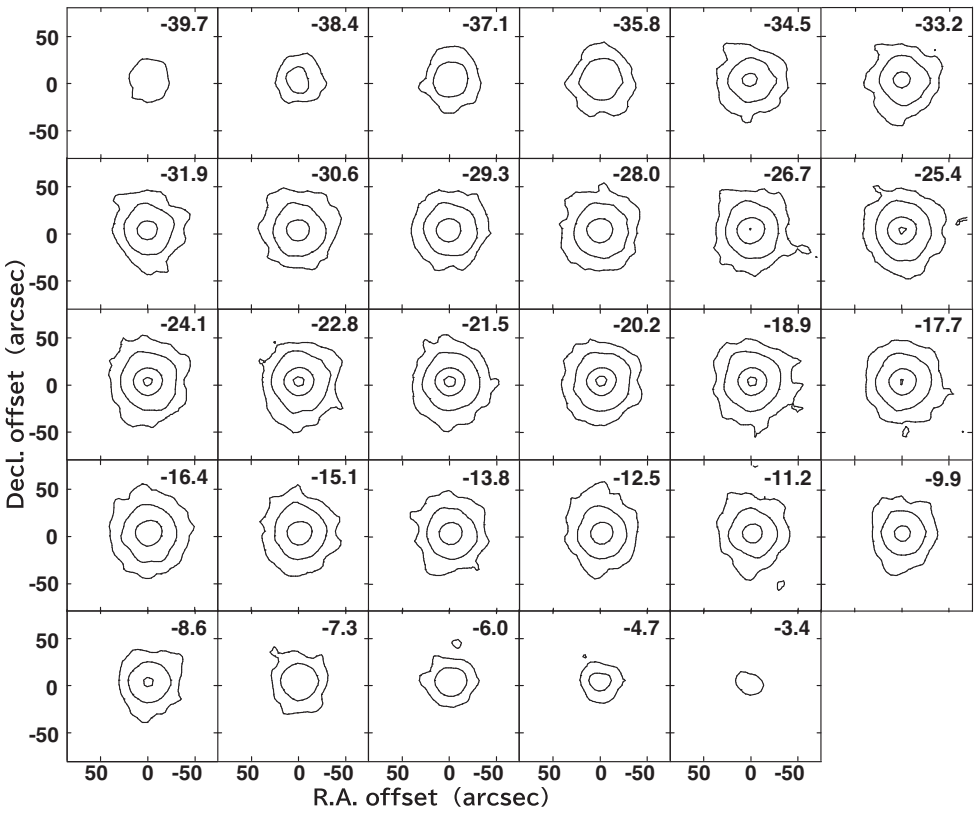

Figure B2. ^{12}CO ($J = 1 \rightarrow 0$) emission channel maps of RAFGL 618. The contour levels are $1\sigma \times$ (3,9,27,47), where 1 σ = 0.06 K.

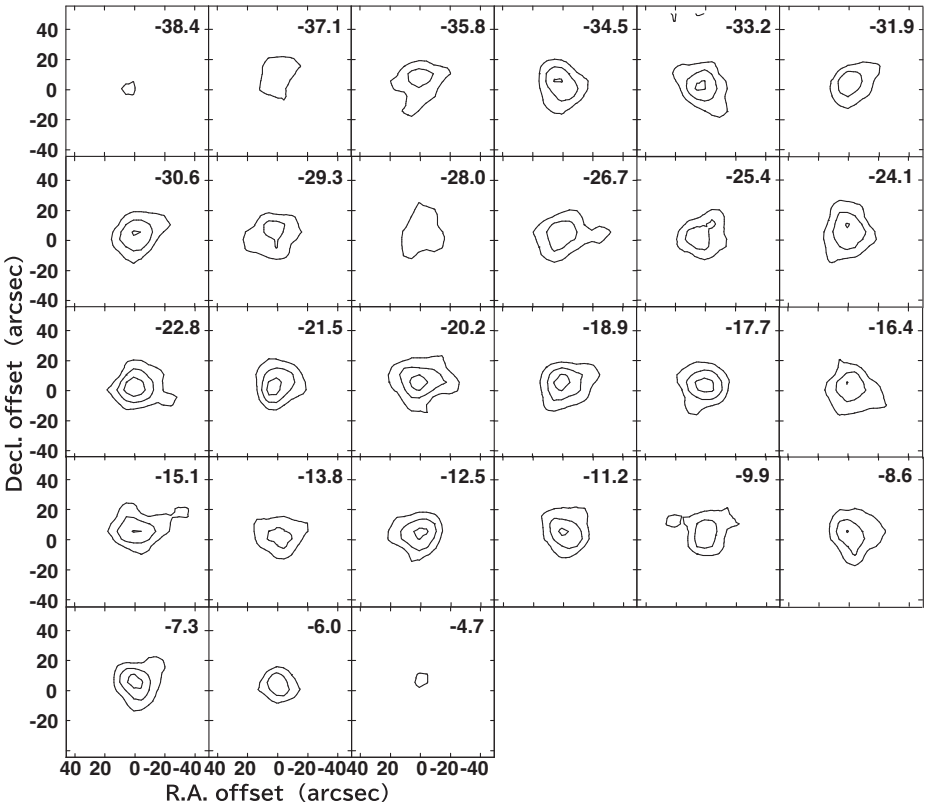

Figure B3. ^{13}CO ($J = 1 \rightarrow 0$) emission channel maps of RAFGL 618. The contour levels are $1\sigma \times$ (3,5,7), where 1 σ = 0.03 K.

[1]*Mizusawa VLBI Observatory, National Astronomical Observatory of Japan, 2-21-1 Osawa, Mitaka, Tokyo 181-8588, Japan*
[2]*Graduate School of Science and Engineering, Kagoshima University, 1-21-35 Korimoto, Kagoshima 890-0065, Japan*
[3]*Center for General Education, Institute for Comprehensive Education, Kagoshima University, 1-21-30 Korimoto, Kagoshima 890-0065, Japan*
[4]*Centre for Astrophysics Research, Department of Physics, Astronomy and Mathematics, College Lane Campus, University of Hertfordshire, Hatfield AL10 9AB, UK*
[5]*Space Science Institute, 4750 Walnut Street, Suite 205, Boulder, CO 80301, USA*
[6]*Institute of Astronomy and Astrophysics, Academia Sinica, 11F of AS/NTU Astronomy-Mathematics Building, No.1, Sec. 4, Roosevelt Rd, Taipei 106319, Taiwan*
[7]*Instituto de Radioastronomía y Astrofísica, UNAM, Antigua Carretera a Pátzcuaro 8701, Ex-Hda. San José de la Huerta, Morelia 58089, Mich., Mexico*
[8]*European Space Agency (ESA), European Space Research and Technology Centre (ESTEC), Keplerlaan 1, NL-2201 AZ Noordwijk, the Netherlands*
[9]*SRON Space Research Organisation Netherlands, Niels Bohrweg 4, NL-2333 CA Leiden, The Netherlands*
[10]*Institut de Ciències de l'Espai (ICE, CSIC), Can Magrans, s/n, E-08193 Cerdanyola del Vallès, Barcelona, Spain*
[11]*ICREA, Pg. Lluís Companys 23, E-08010 Barcelona, Spain*
[12]*Institut d'Estudis Espacials de Catalunya (IEEC), E-08860 Castelldefels, Barcelona, Spain*
[13]*Yunnan Observatories, Chinese Academy of Sciences, 396 Yangfangwang, Guandu District, Kunming 650216, Yunnan, P. R. China*
[14]*Chinese Academy of Sciences South America Center for Astronomy, National Astronomical Observatories, Chinese Academy of Sciences, Beijing 100101, P. R. China*
[15]*Departamento de Astronomía, Universidad de Chile, Casilla 36-D, Camino El Observatorio 1515, 7591245 Santiago, Chile*
[16]*Jodrell Bank Centre for Astrophysics, Department of Physics and Astronomy, School of Natural Sciences, University of Manchester, M13 9PL, Manchester, UK*
[17]*Department of Physical Sciences, The Open University, Walton Hall, Milton Keynes MK7 6AA, UK*
[18]*Institute of Astronomy, KU Leuven, Celestijnenlaan 200D bus 2401, B-3001 Leuven, Belgium*
[19]*UK Astronomy Technology Centre, Royal Observatory, Blackford Hill, Edinburgh EH9 3HJ, UK*
[20]*Department of Physics and Astronomy, University of Western Ontario, London, ON N6A 3K7, Canada*
[21]*Institute for Earth and Space Exploration, University of Western Ontario, London, ON N6A 3K7, Canada*
[22]*SETI Institute, 189 Bernardo Avenue, Suite 100, Mountain View, CA 94043, USA*
[23]*Korea Astronomy and Space Science Institute (KASI) 776, Daedeok-daero, Yuseong-gu, Daejeon 34055, Republic of Korea*
[24]*Department of Physics and Astronomy, University College London, Gower St, London WC1E 6BT, UK*
[25]*Space Telescope Science Institute, 3700 San Martin Drive, Baltimore, MD 21218, USA*
[26]*Max-Planck-Institute for Astronomy, Königstuhl 17, D-69117 Heidelberg, Germany*
[27]*Schmidt Sciences, New York, NY 10011, USA*
[28]*National Science Foundation, 2415 Eisenhower Avenue, Alexandria, Virginia 22314, USA*

This paper has been typeset from a TEX/LATEX file prepared by the author.